An investigation of the accuracy of numerical analysis for modeling free-surface elevation from flow over a shallowly submerged 2D naca0012 hydrofoil

Msc. thesis

G. Sprong

An investigation of the accuracy of numerical analysis for modeling free-surface elevation from flow over a shallowly submerged 2D naca0012 hydrofoil

Msc. thesis

by

G. Sprong

to obtain the degree of Master of Science
at the Delft University of Technology,
to be defended publicly on Thursday December 19, 2019 at 14:00 PM.

Student number:	4149017	
Project duration:	Dec 24, 2018 – Dec 19, 2019	
Thesis committee:	Prof. Dr. ir. J. Westerweel,	TU Delft, Chairman
	Dr. ir. M.J.B.M Pourquie,	TU Delft, supervisor
	Dr. ir. P.R. Wellens,	TU Delft, supervisor
	Ir. K. van der Heiden,	Jumbo Maritime, supervisor
	Dr. ir. H.J. de Koning Gans,	TU Delft, External

An electronic version of this thesis is available at `http://repository.tudelft.nl/`.

TU Delft

JUMBO

Preface

This thesis marks the completion of my Master's program Mechanical Engineering at the Delft University of Technology. This work is the result of hard work at the Jumbo Maritime office and the University. I would like to show my appreciation to the people who have supported me during this work.

I would like to thank Mathieu Pourquie for being my daily supervisor. I have learned a lot from him. It amazes me how involved he has been with the project. I also want to thank Peter Wellens, who has joined several meetings in which he has given valuable insights. Thanks to their input the meetings with Mathieu Pourquie and Peter Wellens have been really productive. Finally, I want to thanks both the external committee member Henk de Koning Gans and Jerry Westerweel, for their effort in reading my thesis and being part of my graduation committee.

Jumbo Maritime has provided me with an graduation subject and a office to work on that project. I am very thankful the past year I was able to work at their office. I want to thank Kasper van der Heiden who has been my supervisor from Jumbo Maritime. His knowledge and guidance during this project have helped me a lot. Apart from all that I have learned at the company, it has been a very pleasant place to work. I would also like the students that have been working besides me at Jumbo maritime, Karel, Gerard, Niels, Michiel, Niek and Job. I want to thank them and Kasper for their company an most of all for the fun discussions we have had.

Lats but not least, I want to thank the people who have sported throughout my studies. These are my Parents, my brother and his girlfriend. Thank you for always being there for me.

G. Sprong
Delft, December 2019

Nomenclature

Abbreviations

Fr_c	Froude number based on chord length
Fr_D	Froude number based basin to hydrofoil height
Fr_h	Froude number based on submergence
Re_m	Reynolds number based on channel mean velocity
Re_δ	Reynolds number based on boundary layer thickness
Re_{u_*}	Reynolds number based on friction velocity
We	Weber number
CFL	Courant Frederich Lewis number
EVM	eddy viscosity model
Re	Reynolds number
RSM	Reynolds stress model

Symbols

α	angle of attack	$^\circ$
α_ω	k$-\omega$ model constant	
β_ω	k$-\omega$ model constant	
δ_{ij}	Kronicker delta	
λ	constant of proportionality	
λ_b	wavelength of the breaking wave	
λ_{t2}	wavelength of the second wave behind the breaker	
μ	kinematic viscosity	$kg/m \cdot s$
ν	dynamic viscosity	$m^{-1} \cdot s^{-1}$
ν_t	eddy viscosity	m^2/s
ω	turbulence dissipation rate	
ω_{log}	turbulence dissipation rate in the log layer	
ω_{vis}	turbulence dissipation rate in the viscous sub-layer	
ϕ	pressure strain correlation	m^2/s^2
ψ	phase fraction	
ρ	density	kg/m^3
τ_{ij}	Reynolds stress tensor	

ε_{ij}	Dissipation	
ξ	sum of elements of the ensemble average	
A	area of the first wave behind the hydrofoil	m^2
a	Amplitude of the second wave behind the hydrofoil	m
a_b	Amplitude of the first wave behind the hydrofoil	m
C_D	drag coefficient	
C_l	lift coefficient	
c_p	heat capacity	$kg \cdot m^2/s^2 \cdot K$
C_ω	specific turbulence dissipation	s^{-1}
$C_{\varepsilon 1}$	k$-\varepsilon$ model constant	
$C_{\varepsilon 2}$	k$-\varepsilon$ model constant	
C_D	closure coefficient	
D^p	diffusion pressure	m^2/s^2
D^v	diffusion velocity	m^2/s^2
E	wall roughness correction factor	
F_1	Blending function	
F_1	k$-\omega$SST transition factor of the blending function	
F_x	force in horizontal direction	
F_y	force in vertical direction	
I	turbulence level of the flow	
k_{ij}	Advection	
L	length of the frontal area of the first wave behind the hydrofoil	m
m	mass flow	kg/s
N	integer number	
P_0	reference pressure	Pa
P_{ij}	Production	
P_{rgh1}	reduced pressure in the undisturbed flow upstream of the hydrofoil	Pa
P_{rgh2}	reduced pressure at any location y beneath the second trough	Pa
P_{rgh}	reduced pressure coefficient	Pa
R^n	residual	
S_{ij}	shear rate	s^{-1}
T_ε	k$-\varepsilon$ blending function	
T_b	frequency of the breaking wave oscillations	s^{-1}
T_m	k$-\omega$SST blending function	

T_ω	k−ωSST blending function	
u'	velocity fluctuations	
u^+	dimensionless velocity	
u_τ	friction velocity	m/s
u_i	element of the ensemble average	
$V_{(t)}$	element volume	m^3
y^+	dimensionless wall distance	
g	gravitational acceleration	m/s^2
h	submergence	m
k	turbulence kinetic energy	m^2/s^2
P	turbulence production	m^2/s^2
t	time	s
U	Flow velocity	m/s
u	local velocity	m/s

abstract

The bulbous bow is a common feature for large displacement vessels. The purpose of the bulbous bow is to reduce the bow wave, hereby making use of wave cancellation theory. The main drawback of these type of bows is that the drag reduction effect is only present for a limited range of sailing speeds. If the transit velocity is altered, the effect of the bulbous bow can even result in an increase of wave making drag. Due to this sensitivity to the sailing speed it is important to be able to predict the location of the waves generated by the protruding bulb.

Computational fluid dynamics is gaining interest in commercial marine industries. The size and transit velocity at which the previously mentioned vessels that employ the protruding bulb operate, results in the common use of Reynolds averaged Navier Stokes (RANS) models. To investigate the accuracy of these RANS models, a 2D model is presented in this thesis. The bulbous bow is modeled as a shallowly submerged 2D naca0012 hydrofoil. The justification for this simplification is that the geometry and flow over a bulbous bow is too complex for the duration of this project. A submerged 2D hydrofoil can still capture the important flow dynamics for free-surface waves.

In this thesis we focused on evaluating the accuracy of RANS models for simulating the wave dynamics that arise when a shallowly submerged 2D naca0012 hydrofoil moves through water. The main objective is to find which geometrical and fluid dynamic properties have an effect on the free surface wave profile. Apart from questioning if these properties have an influence on the wave profile, we also want to know how the wave profile changes by altering these properties.
The interFoam package from OpenFoam was used for simulating the flow. InterFoam adopts the volume of fluid (VOF) approach proposed by Weller (Weller, 2008) for simulating multiphase flows. Turbulence modeling was done using the k-ωSST two equation model from Menter et al. (Menter, 1992).
In 1983 Duncan and his colleagues published a paper on the free surface wave dynamics generated by a towed naca0012 hydrofoil (Duncan, 1983). The results from their experiments are used as a benchmark for the present study.

From a single phase test we found that the experiments from Duncan where performed in the regime where transition of the boundary layer from laminar to turbulent is present. The presence of this transition is expected to be one of the reasons for the disagreement in literature on wave elevation, wavelength zero point crossings and lift and drag coefficients. It is shown that the relatively small gap between the basin floor and the hydrofoil of 0.86 chord lengths has a significant impact on the wave profile and the flow at the hydrofoil. Reynolds independence is found to be at $Re \geq 2 \cdot 10^5$ for a towed hydrofoil submerged at $\frac{h}{c} = 0.955$ with the basin floor located 10 chord lengths below the hydrofoil. Below this value a reduction in Reynolds number results in an decrease of the wave amplitude and an increase in the wavelength.
The assumption to neglect the resistance from the hydrofoil wake made by Duncan is shown to be false. The dominating dimensionless parameters for these types of flows are: Froude based on submergence Fr_h, Froude based on basin to foil height Fr_D and the Reynolds number based on the chord length and the bottom fluid parameters Re_c. Note that in this thesis the angle of attack (α) has been kept constant at 5° which does effect the flow but this has not been investigated during this research.

A attempt is made to simulation breaking waves in the present model. The Breaker type in the present study differs from the one found by Duncan et al. (Duncan, 1983). Even if the same breaker type was found the elevation and wavelength differ a lot. It is therefore concluded that The present model is not suited for predicting breaking waves.

Contents

List of Figures

List of Tables

1 Introduction

1.1. Problem description

Free-surface waves induced by submerged objects arise in a wide range of engineering fields. An abundance of theoretical work published, proves the relevance of this topic. Within marine engineering free-surface waves are responsible for dynamic loading on offshore structures, stability of floating structures, added drag for ships in transit, among others. Added drag is the motivation for this study. large displacement vessels induce elevation of the free-surface between seawater and air. This flow behavior contributes to the total drag such vessels encounter. Generation of waves, commonly referred to as wave making resistance is accountable for up to 20% of the total resistance for this type of ships(Te Chow, 2013). Within marine engineering drag reduction is continually under investigation. Even a slight improvement of the ships resistance has much impact on traveling expenses. This is due to the shear size of these vessels, together with the distance they travel. The increasingly demanding emission regulations, and lack of "green" alternatives also push the industry to become more fuel efficient. One often utilized drag reduction solution is the Bulbous bow.

Figure 1.1: picture of a container vessel equipped with a bulbous bow. Ridley (2014)

The bulbous bow is an extension at the bow of the vessel. This extension is completely submerged while in in transit. The submerged bulb generates a free surface wave, which is designed such that the bow wave and the bulb wave are in counter phase. This results in a reduced height of the wave profile along the hull of the vessel. The bulb of a bulbous bow is designed such that the lift generated at the bulb is maximized while the drag is minimized.

1.2. Jumbo Maritime

Jumbo Maritime is a heavy lift shipping and offshore transportation & installation contractor. The operational fleet all use a protruding bulb to reduce wave making drag. With an eye on the future the question arises whether to maintain this bow shape.

Due to the increasing importance of numerical simulation in the marine industry Jumbo Maritime is interested is using computational fluid dynamics (CFD) to evaluate such problems.
To answer such questions, the performance of current numerical simulations needs to be evaluated. In this thesis a 2-D hydrofoil is used to model free surface effect as encountered by vessels equipped with a bulbous bow. Model tests performed by Duncan et al.(Duncan, 1983) are used to validate the model.

1.3. Approach

This thesis presents a numerical model to predict the free-surface elevation from a 2D naca0012 hydrofoil which is shown in figure 1.2

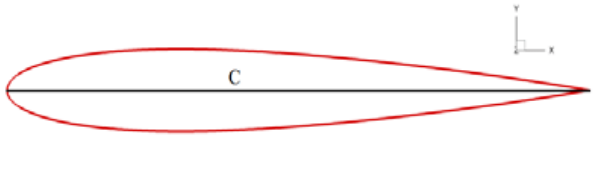

Figure 1.2: naca0012 geometry, c is the chord length. Mahboubidoust u. a. (2015)

This simplification is justified by the complexity of the geometry and the cumbersome numerical schemes that are necessary for two phase flow. A hydrofoil is chosen, because this is the closest 2-D representation of a bulbous bow separated from the bow. The principle of a submerged hydrofoil is similar, the lift is maximized while the drag is minimized. It is important to note that this simplification poses strong limitations in drawing conclusions about the complex 3-D geometry that comes with the bulbous bow. Nevertheless, the proposed model can be used to identify which properties and dimensionless numbers dominate the wave characteristics. For this reason the analysis in this thesis is performed by changing one property of the flow at a time. The objective of this thesis is summarized in the following research question:

> How do relevant fluid and geometrical properties effect the wave profile generated by a shallow submerged naca0012 hydrofoil?

To answer this research question a number of subquestions are formulated that serve as a guidance towards answering the research question above.

> What grid dimensions and domain sizes are necessary for accurate representation of the flow?
>
> How does the wave profile respond to different Reynolds numbers?
>
> To what degree does turbulence in the mean flow effect the final wave train?
>
> What effect does the submergence of the hydrofoil have on the wave dynamics?
>
> How accurate is the representation of breaking waves using RANS models?

1.4. Thesis structure

The proposed thesis, is build up as follows. Firstly the mathematical background from the numerical method is given in chapter 2. At the end of this chapter the methods for mesh setup and post processing are discussed. Chapter 3, discusses the numerical tests performed to investigate the research questions. This is done by firstly modeling a fully developed channel to test the chosen turbulence model and investigate the influence of the mesh resolution in close proximity of the wall. Thereafter a single phase airfoil model is compared with existing data form several authors. A grid dependency study is performed to eliminate grid effects from this study. Finally the two phase model is validated against the experiments from Duncan et al. (Duncan, 1983), and compared against other paperers that tried to model after this experiment. In chapter 4 a final discussion is presented in which the above mentioned research questions and subquestions are answered.

2

Related work

2.1. Introduction

In this thesis an attempt is made to reproduce the experiments performed by Duncan and his colleagues (Duncan, 1983). This reproduction is done numerically using openFoam. The experiment from Duncan is chosen because of the number of citations. Even in recent studies this article is often used as a source of experimental data. Moreover the number of experiments performed in this field are limited.
The aim of this section is to explain the experiment from Duncan et al. and to give an overview of studies that aim to reproduce the data from Duncan et al.

2.2. Experiment Duncan

The experiment from Duncan was performed by towing a shallowly submerged naca0012 hydrofoil in a calm water basin. The movement of the hydrofoil creates disturbances at the free-surface. Duncan used a camera to capture the free surface. There are two resulting free surface profiles which are of importance is this theses. The first of which is a stationary wave train, depicted in figure 2.1a. The other is a so called spilling breaker, depicted in 2.1b. A spilling breaker is defined by a unstable top which spills over the wave, without the wave collapsing completely.

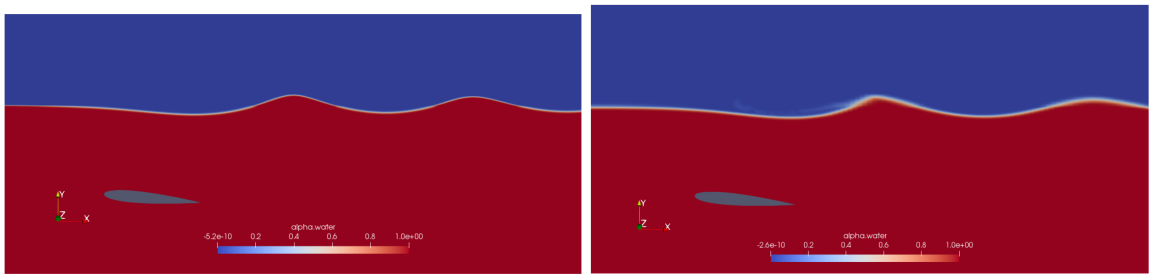

(a) example of a non-breaking stationary wave train, generated by a submerged naca0012 hydrofoil.

(b) example of a spilling breaker and resulting wave train, generated by a submerged naca0012 hydrofoil.

Figure 2.1: Contour of volume fraction

The experiment was carried out at fixed Froude numbers based on the chord length of the hydrofoil of ($Fr_c = \frac{U}{\sqrt{(g \cdot c)}}$) $Fr_c = 0.425, 0.567, 0.709$. The foil is positioned at a fixed height of $\frac{d}{c} = 0.86$ above the floor of the basin. The submergence of the hydrofoil was changed by pumping water into the basin. A schematic representation is given in figure 2.2. Note that the reference frame in figure 2.2 is fixed to the hydrofoil, where in the actual experiment the basin is fixed and the hydrofoil is moving. This representation is chosen because the numerical simulations adopt the same reference frame.

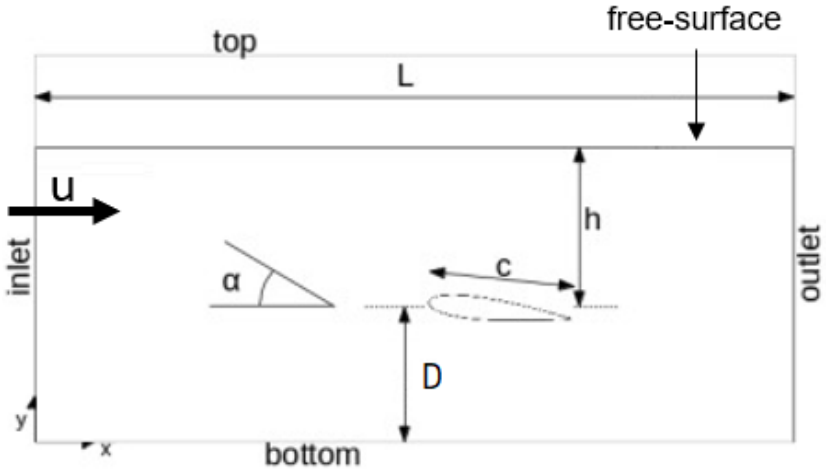

Figure 2.2: schematic representation of the experimental setup from Duncan et al. (Duncan, 1983), from a reference frame fixed to the hydrofoil. d is the depth of the basin measured from the hydrofoil center-line. h is the submergence level also measured from the of the foil. c is the chord length of the hydrofoil. Note that $y = 0$ is at the free-surface and $x = 0$ at the center of the hydrofoil.

The experiments were performed for $Re \approx 2 \cdot 10^5$. Flow over an naca0012 hydrofoil at an angle of attack of 5° at $Re \approx 2 \cdot 10^5$ shows transition of the boundary layer regime from laminar to turbulent. (Yousefi und Razeghi, 2018).
Duncan assumes deep water regime to neglect the effect of the floor of the basin on the waves at the free-surface. Duncan notes that the floor does effect the lift of the foil. He also points out that the acceleration history of the towed foil does effect the final wave train. Duncan evaluated the wave resistance from his experiment using a momentum balance over two measurement point in the flow. The first measuring point lies upstream of the hydrofoil and the second lies at the second trough of the free surface wave train. In his calculations Duncan assumes that wake resistance from the foil can be neglected. Another statement he makes is that for non-breaking waves, potential flow theory can accurately describe the flow.
There are a couple of drawbacks that come with the decision of comparing against Duncan's article. There is no axis system given where the location of the hydrofoil in horizontal direction is specified. Vertical velocity distribution and head defects are only given for breaking cases. Th head defect is the difference the total head at the measuring point and the total head in the undisturbed flow upstream of the hydrofoil. It turned out that breaking waves are difficult to model. This is later discussed in section 4.4.3
De Blasi et al. (De Blasi und Romano, 2000) tried to repeat the experiments from Duncan and his colleagues (Duncan, 1983). De Blasi used a circulating water channel for the experimental setup. The dimensionless numbers from de Blasi's experiment were: $Fr_c = 0.567$ and $Re \approx 1 \cdot 10^6$. Note that for this setup transition of the boundary layer regime is expected to be instantaneous at the stagnation point. De Blasi concludes that the circulating water channel creates an undesired free surface boundary layer in the water phase which influences their result. The effect of this boundary layer is that breaking of waves happens earlier than in the experiments from Duncan et al. (Duncan, 1983).If there is no breaking wave, the free surface boundary layer is said to reduce the trailing wave amplitude and wave length. De Blasi compared the result from their own study and those from Duncan et al. (Duncan, 1983) against a desingularized boundary integral formulation from Lalli et al. (Lalli, 1997). In this potential method the free surface boundary layer is modeled as an inviscid rotational inflow. Using this numerical model they could reproduce the experimental results relatively accurately. Since potential methods do not solve viscous effects (Kundu, 2013) it is expected that the wave profile is slightly over predicted. De Blasi et al. (De Blasi und Romano, 2000) does not explain if and how they compensated for the over prediction of potential methods.

2.3. Numerical studies

Next follows a discussion of studies that tried to reproduce the experiment from Duncan et al. (Duncan, 1983) numerically. Within literature there are two numerical approaches that are often used for modeling free surface waves generated by a submerged hydrofoil. These two are potential flow or RANS. The experiments discussed above have been modeled by many researchers using different types of numerical simula-

tions. A number of these studies are chosen to compare against the present model: Chen and Chwang (Chen, 2012), Lupieri and Contento (Lupieri und Contento, 2015) Walker et al.(Walker u. a., 2004), Di Mascio et al. (Di Mascio u. a., 2007) and Prasad et al. (Prasad u. a., 2015). Table 2.1 lists model parameters for each of these simulations. In table 2.1 the simulation program and turbulence model is given. The y^+ range along the face of the hydrofoil is also listed together with the wall treatment for k. The − sign indicates that this quantity is either not used in the given model or it is not documented.

Table 2.1: Model parameters used by reference articles (Chen, 2012, De Blasi und Romano, 2000, Di Mascio u. a., 2007, Lupieri und Contento, 2015, Walker u. a., 2004) and the present study. For modeling the shallow submerged hydrofoil flow.

	program	turbulence model	y^+ range	k wall
present	OpenFOAM	k-ωSST	$0.052 - 0.67$	0
Prasad	OpenFOAM	k-ε	$5 - 10$	kqRWallFunction
Lupieri	OpenFOAM	k-ωSST	5	−
Walker RANS	CFDSHIP-IOWA	k-ε or RSM	−	−
Walker potential	de-singularised potential method	−	−	−
Di Mascio	written Navier-Stokes solver	Spalart and Allmaras	0.5	−
Chen	written Navier-Stokes solver	−	−	−

A general underestimation of the wave profile from Duncan et al. (Duncan, 1983) is documented by the reference articles that adopt a RANS model. This underestimation was not found by Lupieri et al. (Lupieri und Contento, 2015). Lupieri documents an underestimation of the first hollow and an overestimation of the first crest. Lupieri argues that the difference in crest height is associated with turbulence production and dissipation occurring in different parts of the trailing wave. Lupieri also claims that RANS models are not able to correctly predict pressure in the suction zone of the hydrofoil.

Potential methods are expected to show an overestimation of the wave elevation. Potential flow models, like the one proposed by Walker et al. (Walker u. a., 2004) do not model viscous effects. Neglecting viscous effects results in an overall overestimation of the wave profile. (Walker u. a., 2004)

Chen and Chwang (Chen, 2012) present a wave profile for $Re = 3 \cdot 10^4$ which is surprisingly similar to the model results from Duncan et al.(Duncan, 1983) ($Re = 2 \cdot 10^5$), even though the Reynolds number is significantly lower. Since this contradicts with what we expect a thorough investigation on results from Chen and Chwang is given in section 4.4.2.
Lupieri (Lupieri und Contento, 2015) and Walker (Walker u. a., 2004) both discuss the effect of the domain size on the wave elevation. Walker does discuss the effect of increasing cell sizes towards end of the domain. If this increase is to close to the region of interest, attenuation of waves can be amplified. While walker only mentions the importance of the domain size and shows the effect a bad grid can have on the results, Lupieri has tested multiple domain sizes and advises to use 20 chord lengths upwind and 40 chord lengths downwind. Both adopt a sponge layer at both ends of the domain. A sponge layer is a region in which the free-surface waves are artificially dampened to prevent reflection of waves from domain edges. The effect of domain size and sponge layers is further discussed in section 4.4.2 Multiphase non-breaking.

3

Background

3.1. Axis system

Figure 3.2 represents the coordinate system used in this thesis.

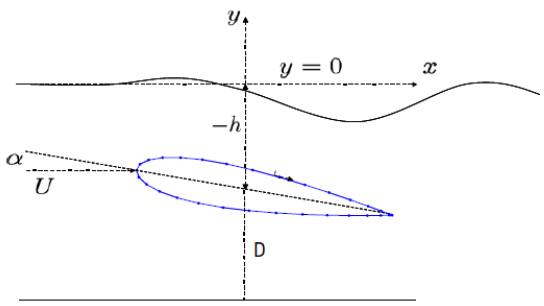

Figure 3.1: Illustration of the model with corresponding coordinate system. With a fixed coordinate system x and y. Attack angle (α) and submergence h. U represents the velocity of the flow. Chen (2012)

3.1.1. Dimensionless numbers

Dimensional analysis is used to identify the relation between governing parameters of a system. To obtain the dimensionless numbers that describe a model all variables from the model are listed in table 3.1

Table 3.1: List of the variables that describe the flow over a shallow submerged hydrofoil and their units. h is the submergence of the hydrofoil. C is the chord length, D is the distance between the hydrofoil and the bottom of the basin, g is the gravitational acceleration, μ_w is the dynamic viscosity of water, μ_a is the dynamic viscosity of air, ρ_w is the density of water, ρ_a is the density of air and σ is the surface tension between air and water.

	h	c	D	U	g	μ_w	μ_a	ρ_w	ρ_a	σ
Mass (kg)	–	–	–	–	–	1	1	1	1	1
Length (m)	1	1	1	1	1	−1	−1	−3	−3	–
Time (s)	–	–	–	−1	−2	−1	−1	0	0	−2

From Table 3.1 we see that the present problem is governed by 10 different parameters which consist of three different units. This tells us that the problem is described by seven different dimensionless parameters. The seven parameters are given and explained below.

The experiments performed by Duncan et al. (Duncan, 1983) used the Froude number based on the chord length of the hydrofoil. From the geometry of the experimental setup, two additional length scales are mentioned which probably influence the flow. These are the submergence h and the depth of the channel D. Nu-

merical studies often neglect the depth of the basin, this is further discussed in section 4.4. The corresponding Froude are the first three dimensionless parameters that describe the flow from Duncans experiment.

$$Fr_c = \frac{U}{\sqrt{(g \cdot c)}} \tag{3.1}$$

$$Fr_{h\,mean} = \frac{U}{\sqrt{(g \cdot h)}} \tag{3.2}$$

Apart from the Froude number the surface tension and viscosity can also effect the flow. Associated dimensionless numbers are given below.

$$Fr_D = \frac{U}{\sqrt{(g \cdot D)}} \tag{3.3}$$

Apart from the Froude number the surface tension and viscosity of water can also effect the flow. Associated dimensionless numbers are given below.

$$Re = \frac{U \cdot c}{\nu_w} \tag{3.4}$$

$$We = \frac{\rho \cdot c \cdot U^2}{\sigma} \tag{3.5}$$

The last two dimensionless numbers give the ratio between the properties of the two fluids that are present. the first is the viscosity ratio

$$\kappa = \frac{\mu_a}{\mu_w} \tag{3.6}$$

$$\eta = \frac{\rho_a}{\rho_w} \tag{3.7}$$

3.2. Mathematical background

This study adopts the k$-\omega$SST Reynolds averaged Navier Stokes (RANS) model, in combination with a volume of fluid (VOF) method for capturing the free surface. The mathematical background of these models is explained in this section.

The continuity equation given below states the conservation of mass.

$$\frac{\partial \rho}{\partial t} + \nabla \cdot (\rho u) = 0 \tag{3.8}$$

Typical velocities in the present model are such that compressibility effects can be neglected. The incompressibility assumption together with mass and momentum balance allow the derivation of the incompressible Navier-Stokes equation.

$$\rho\Big(\frac{\partial u}{\partial t} + (u \cdot \nabla) u\Big) = \rho g - \nabla p + \mu \nabla^2 u \tag{3.9}$$

The incompressible continuity equation is given as follows.

$$\nabla \cdot u = 0 \tag{3.10}$$

In dimensionless form equation 3.9 becomes

$$\frac{\partial u}{\partial t} = (u \cdot \nabla) u = g - \nabla p + \frac{1}{Re} \nabla^2 u \tag{3.11}$$

Solving equation 3.9 using Direct numerical simulation (DNS) results in an exact representation of the flow. Direct numerical simulation for this model is costly. For this reason modeling of the Navier stokes equations is performed.

3.2.1. Numerical approximation

In this thesis modeling of the flow over a submerged hydrofoil is done using Reynolds averaging for the Navier-Stokes equations. The ensemble averaged solution $\langle u_i \rangle$ is calculated as follows

$$\langle \underline{u}_i \rangle = \frac{1}{N} \sum_{\mu=1}^{N} u_i|_\mu \tag{3.12}$$

Here i ($\underline{u}_i, i = 1, .., n$) represent the element of the ensemble and μ is the sum of the elements.

Decomposition of the average in the mean value and the fluctuation

$$u_i = \langle u_i \rangle + u_i' \tag{3.13}$$

The incompressible Navier-Stokes equations for the average are given in vector form.

$$\frac{\partial \underline{u}}{\partial t} + \nabla \cdot (\langle \underline{u} \rangle \langle \underline{u} \rangle) + \frac{1}{\rho} \nabla \langle p \rangle - \frac{1}{Re} \nabla \cdot \nabla \langle \underline{u} \rangle = -\nabla \cdot \langle \underline{u}' \underline{u}' \rangle \tag{3.14}$$

$$\nabla \cdot \langle \underline{u} \rangle = 0$$

Apart form velocity and pressure, the velocity fluctuations are also present in this equations in the form of an unknown quantity. The velocity fluctuations add an additional unknown to equation 3.14. This additional unknown makes that equation 3.14 contains more unknown variables than equations and can therefore not be solved directly. This is the closure problem. To overcome this problem turbulence models are used.

3.2.2. turbulence modeling

Turbulence models approximate the matrix on the right hand side (RHS) of equation 3.14. This is called The Reynolds stress tensor.

$$\tau_{ij} = -\langle u_i' u_j' \rangle \tag{3.15}$$

The conservation law for the Reynolds stress tensor is the Reynolds stress transport equation (RST), with the general form

$$\frac{\partial \langle u_i' u_j' \rangle}{\partial t} + \underbrace{k_{ij}}_{Advection} = \underbrace{P_{ij}}_{Production} + \underbrace{T_{ij} + D_{ij}^{v} + D_{ij}^{p}}_{Diffusion} + \underbrace{\Phi_{ij}}_{Pressure\,strain\,correlation} - \underbrace{\varepsilon_{ij}}_{Dissipation} \tag{3.16}$$

Turbulence models that are commonly used are eddy viscosity models (EVM) or Reynolds stress models (RSM). This thesis focuses on eddy viscosity models. The justification for this decision lies in the computational requirements and stability. Where EVM solve for one or two transport equations RSM does this for at least six. Despite being more accurate, RSM models have slower convergence and can be unstable.(Hickel, 2018)

Eddy viscosity models are based on the hypothesis that turbulence causes momentum exchange between fluid elements. The model estimates the Reynolds stress from the mean shear rate. The proportionality is named eddy viscosity (ν_t).

$$\langle u_i' u_j' \rangle \cong 2\nu_t S_{ij} - \frac{2}{3}\delta_{ij} k \tag{3.17}$$

Here S_{ij} represents the shear rate(viscous forces between fluid particles)and k is the turbulence kinetic energy. Substitution of equation 3.17 in equation 3.14 gives:

$$\frac{\langle u_i \rangle}{\partial t} + \langle u_j \rangle \frac{\langle u_i \rangle}{\partial x_j} = \frac{\partial}{\partial x_i}\left(\frac{\langle p \rangle}{\rho} + \frac{2}{3} k \right) + \frac{\partial}{\partial x_j}(2(\nu + \nu_t) S_{ij}) \tag{3.18}$$

This thesis makes use of a two equation EVM based on two industry standard two equation models. Two equation models solve for two extra transport equations. Distinction between models of this sort is the kind of transport variables for which an equation is introduced. The present study uses a model called $k-\omega$ shear stress transport (SST). This model combines two other models based on their free stream accuracy and near wall treatment.

The first of these two models is the $k-\varepsilon$ two equation model from Jones & Launder. This turbulence model solves transport equations for turbulent kinetic energy (k) and turbulent dissipation (ε). Transport equations are derived from the assumption of an equilibrium between turbulence production and dissipation.
The following equation is called the eddy viscosity equation and it gives the relation of k and ϵ

$$\nu_t = C_D \frac{k^2}{\varepsilon} \tag{3.19}$$

C_D is the closure coefficient which is case dependent. The closure coefficient value was found to give acceptable results if chosen between 0.07 and 0.09. (Wilcox u. a., 1998) Jones & Launders $k-\varepsilon$ model solves a partial differential equation for turbulence kinetic energy as follows

$$\frac{\partial k}{\partial t} + \langle u_j \rangle \frac{\partial k}{\partial x_j} = \tau_{ij} \frac{\partial \langle u_i \rangle}{\partial x_j} + \frac{\partial}{\partial x_j}\left(\left[\frac{1}{Re} + \frac{\nu_t}{Pr_k}\right]\frac{\partial k}{\partial x_j}\right) - \varepsilon \tag{3.20}$$

A transport equation for the turbulence dissipation rate is solved as well

$$\frac{\partial \varepsilon}{\partial t} + \langle u_j \rangle \frac{\partial \varepsilon}{\partial x_j} = C_{\varepsilon 1}\frac{\varepsilon}{k}\tau_{ij}\frac{\partial \langle u_i \rangle}{\partial x_j} + \frac{\partial}{\partial x_j}\left(\left[\frac{1}{Re} + \frac{\nu_t}{Pr_\varepsilon}\right]\frac{\partial \varepsilon}{\partial x_j}\right) - C_{\varepsilon 2}\frac{\varepsilon}{k}\varepsilon \tag{3.21}$$

A lack in accuracy for near wall modeling was found. This is caused by inconsistency in the way the model handles pressure diffusion in the equation for k. (Bernard, 1986)

A two equation model that achieves better results in near wall situations is the $k-\omega$ model from Wilcox (Wilcox, 1988) Wilcox assumed the specific turbulence dissipation (ω) to be related to the ratio of ε and k.

$$\nu_t = \frac{k}{\omega} \tag{3.22}$$

$$\omega = \frac{1}{C_D}\frac{\epsilon}{k} \tag{3.23}$$

The two transport equations for $k\&\omega$ as defined by Wilcox (Wilcox, 1988)

$$\frac{\partial k}{\partial t} + \langle u_j \rangle \frac{\partial k}{\partial x_j} = \tau_{ij} \frac{\partial \langle u_i \rangle}{\partial x_j} + \frac{\partial}{\partial x_j}\left(\left[\frac{1}{Re} + \frac{\nu_t}{Pr_k}\right]\frac{\partial k}{\partial x_j}\right) - C_D k\omega \tag{3.24}$$

$$\frac{\partial \omega}{\partial t} + \langle u_j \rangle \frac{\partial \omega}{\partial x_j} = \alpha_\omega \frac{\omega}{k}\tau_{ij}\frac{\partial \langle u_i \rangle}{\partial x_j} + \frac{\partial}{\partial x_j}\left(\left[\frac{1}{Re} + \frac{\nu_t}{Pr_\varepsilon}\right]\frac{\partial \omega}{\partial x_j}\right) - \beta_\omega \omega^2 \tag{3.25}$$

In 1992 Florian Menter proposed a model which combines the $k-\omega$ and $k-\varepsilon$ models.(Menter, 1992) The SST model applies the Wilcox $k-\omega$ model in the first 50% of the boundary layer after which it transitions towards the Jones & Launder $k-\varepsilon$ model. Transition between both models happens in the outer 50% of the boundary layer. Menter named the transition factor the blending function F_1. Transition is mathematically denoted as follows.

$$T_m = F_1 T_\varepsilon + (1 - F1) T_\omega \tag{3.26}$$

Here T_m, T_ε and T_ω are Menter's $k-\omega SST$, Launders $k-\varepsilon$ and wilcox his $k-\omega$ model respectively. The blending function

$$F_1 = tanh(max(min\Big(\frac{\sqrt{k}}{0.09\omega y}; 0.45\frac{\omega}{\Omega}\Big); \frac{400\nu}{y^2\omega}) \tag{3.27}$$

$$\frac{\partial k}{\partial t} + \langle u_j \rangle \frac{\partial k}{\partial x_j} = \tau_{ij} \frac{\partial \langle u_i \rangle}{\partial x_j} + \frac{\partial}{\partial x_j}\left(\left[\nu + \sigma_k \nu_T\right]\frac{\partial k}{\partial x_j}\right) - C_D k\omega \tag{3.28}$$

$$\frac{\partial \omega}{\partial t} + \langle u_j \rangle \frac{\partial \omega}{\partial x_j} = \alpha \frac{\omega}{k}\tau_{ij}\frac{\partial \langle u_i \rangle}{\partial x_j} + \frac{\partial}{\partial x_j}\left(\left[\nu + \sigma_k \nu_T\right]\frac{\partial \omega}{\partial x_j}\right) - \beta\omega^2 + 2(1-F_1)\sigma_{\omega 1}\frac{1}{\omega}\frac{\partial k}{\partial x_i}\frac{\partial \omega}{\partial x_i} \tag{3.29}$$

3.2.3. Multiphase modelling

In numerical simulations the free-surface boundary is formulated either by a boundary or volume formulation Tsai und Yue (1996). Boundary methods are better suited for inviscid irrotational flows. Volume discretisation can be used for inviscid and viscous flows. The Volume of Fluid (VOF) method Hirt and Nichols Hirt und Nichols (1981) formulated is a volume formulation applied in discretization schemes. The main idea behind this method is that for discretization it is computationally more stable to define fluid regions than exactly define the boundary interface. The disadvantage of fluid regions is that much more data has to be stored to define fluid regions. VOF solves a transport equation for the volume fraction within cells. The interface representation from VOF is limited by the grid size. To overcome this limitation interface sharpening methods are used. VOF methods solve a single momentum equation based on the fluids mixture properties. A surface tension force (F_s) is implemented to separate the phases. The surface tension force is defined by the surface tension parameter (σ) and the local curvature of the interface ($\kappa(x)$).

$$\frac{\partial \rho U}{\partial t} + \nabla \cdot (\rho UU) = -\nabla(p) + \nabla \cdot (\mu(\nabla(U) + \nabla(U)^T)) + \rho g + F_s \tag{3.30}$$

$$F_s = \sigma \kappa(x) n, \quad n = \nabla\psi / |\nabla x|, \quad \kappa(x) = \nabla \cdot n$$

Interface sharpening for phase fraction calculation is done using the method proposed by Weller. Weller (2008) This method adds an extra compression term to the left hand side (LHS) of the volume fraction transport equation. This compression term is formulated as a compression velocity $\vec{u}_c$ normal to the interface. The phase fraction in represented by ψ_k.

$$\nabla \cdot (\vec{u}_c \psi_k (1 - \psi_k)) = 0 \tag{3.31}$$

$\psi_k(1-\psi_k)$ is implemented to ensure compression is only applied on the interface. The volume fraction transport equation then becomes equation 3.32.

$$\frac{\partial \psi_k}{\partial t} + \vec{u}_k \cdot \nabla \psi_k + \nabla \cdot (\vec{u}_c \psi_k (1 - \psi_k)) = 0 \tag{3.32}$$

Discretisation is performed by applying bounded differencing. The compression velocity is given as follows.

$$\vec{u}_c = \min(C_\psi |\vec{u}|, \max(|\vec{u}|)) \frac{\nabla \psi}{|\nabla \psi|} \tag{3.33}$$

$\frac{\nabla\psi}{|\nabla\psi|}$ is the unit normal vector on the interface and C_ψ is a coefficient used to control the compression. When C_ψ is a binary number, equation 3.32 reduces to.

$$U_r = C_\psi |\vec{u}| \frac{\nabla \psi}{|\nabla \psi|} \tag{3.34}$$

In openFoam there are multiple multiphase solvers based on the VOf method. The distinction between them is based on whether there is a sharp interface between the fluids or not.

1. InterFoam, this solver is developed for modeling of immiscible fluids with a sharp interface. The phase distinction is determined using VOF method.
2. Eulerian multi fluid method Solver for dispersed flows with high volume fractions of both fluids.
3. Eulerian -Lagrangian method Another solver for dispersed flows but this solver is better suited for flows in which the dispersed phase has a low volume fraction
4. hybrid VOF or multifluid method This model is used for complex flows in which a sharp interface is present as well as dispersed phases.

In condition that waves do not break,the interFoam method should be used. Evaluation of this solver was done by Deshpande et al.Deshpande u. a. (2012). For inertia dominated flows with density ratios ~ $O(10^3)$, the solver showed excellent agreement to experimental and analytical data. The model converged to a solution which deviated 10% from the analytically resolved curvature. Computation time for free-surface flows is considerably longer than for single phase flows. The increase in computation time is due to the small mesh size necessary to resolve large droplets. Also, interface capturing methods are bound to explicit solutions which require Courant number (C_{fl}) of $O(0.25)$Wardle und Weller (2013).

3.2.4. y^+

Close to walls the velocity gradient is large. This is called the near-wall region. To accurately model wall shear and turbulence production, the height of the first grid cells at the wall are limited. The height of these cells are computed using the non-dimensional y^+ value. y^+ relates the cell height to the flow parameters.

$$y^+ = \frac{u_\tau}{\nu} y \tag{3.35}$$

$$u_\tau = \sqrt{\frac{\tau_w}{\rho}} \tag{3.36}$$

$$u^+ = \frac{u}{u_\tau} \tag{3.37}$$

The non dimensional value y^+, is a function of the friction velocity u_τ and the viscosity ν. An other quantity often used in CFD is the dimensionless velocity u^+. This value is used within the aforementioned near-wall region, and relates the velocity field to the friction velocity.
Within the near-wall region fluid flow is dominated by viscous and turbulent stresses. The relative contribution of these phenomena is dependent on the distance from the wall. For this reason the near-wall region is divided in three sub-regions.

1. Viscous sublayer, The region closest to the wall is dominated by viscous effects. In the range of $0 < y^+ < 5$ the shear stress in the fluid is approximately equal to the wall shear stress. In this region the velocity gradient is constant and is given by

$$u^+ = y^+ \tag{3.38}$$

2. Logarithmic layer, Further away from the wall, $(30 < y^+ < 300)$ the velocity profile is dominated by turbulent stress. Changes in velocity profile are slow and this is described by logarithmic relation.

$$u^+ = \frac{1}{\kappa} ln(Ey^+) \tag{3.39}$$

   Here κ is the Von Karman constant with a value of 0.41 and E is a wall roughness correction factor. 9.8 is used for smooth walls.

3. Buffer layer, In the region between the viscous sub-layer and the logarithmic layer, turbulence stress and wall shear are of equal influence on the flow profile. This region is more difficult to approximate mathematically. To avoid uncertainties a grid should be made with the first cell center outside of this region.

To avoid modeling within the buffer zone, a grid should have a wall spacing that satisfies either $y^+ < 1$ or $30 < y^+ < 300$.

3.2.5. Boundary conditions

On each edge in the domain a boundary condition is specified for the velocity , volume fraction pressure and turbulence properties ω and k. We do this for the inlet, outlet, airfoil, bottom , Top. At the top a symmetry plane is assumed for all parameters.

U

At the inlet a fixed value for both fluid streams is specified, which is case dependent. In the base case the velocity U is $1.7765 m/s$. besides that a no slip wall is imposed at the hydrofoil, this sets the velocity at the wall to $0 \frac{m}{s}$. At the bottom of the geometry a free slip boundary condition is used. At the outlet the outletPhaseMeanVelocity boundary condition is used. The outletPhaseMeanVelocity allows the user to specify a mean velocity at the outlet, the volume fraction is than changed such that mass conservation is fulfilled.

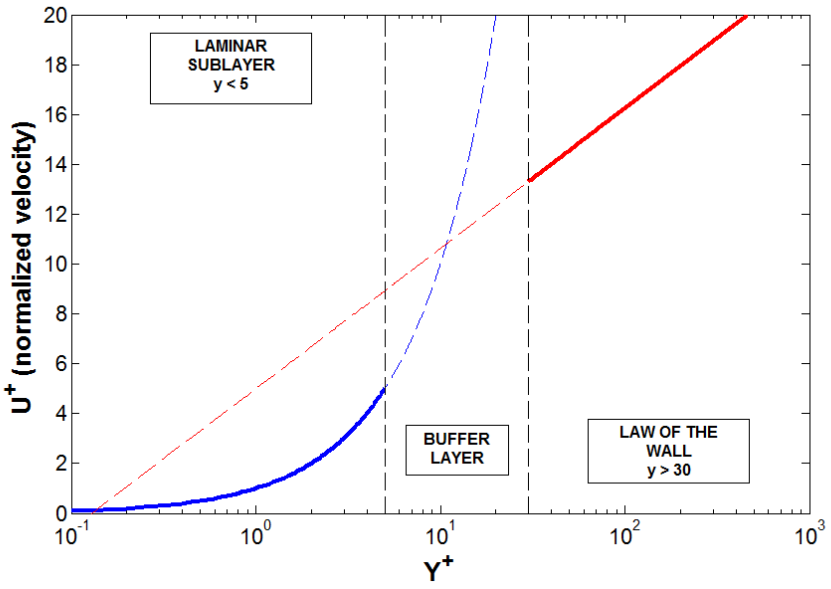

Figure 3.2: Normalized velocity plotted against the dimensionless wall spacing. graphically depicting the linear profile in the laminar region and the exponential growth in the logarithmic layer. In the buffer layer an extrapolation of both lines is visible thereby showing the reason this region should be avoided in grid generation.

ω

ω is the specific dissipation rate. Near a wall the fluid decelerates towards $0\frac{m}{s}$ dissipation of momentum into heat is large at this boundary. For this reason a wall function must be specified. Within OpenFoam the omegaWallfunction boundary conditions should be used when that boundary represents a wall. The OmegaWallFunction from OpenFoam automatically combines the viscous and log layer representation of the near wall region. This is done as follows.

$$\omega = \sqrt{\omega_{Vis}^2 + \omega_{Log}^2} \tag{3.40}$$

Here ω_{Vis} represents the dissipation rate within the viscous sublayer and ω_{Log} represents the dissipation within the loglayer. The OmegaWallFunction is used the the bottom and the airfoil. At the inlet a fixed value is used. the oulet adopts the inletOutlet boundary condition from openFoam, which simply copies the inlet condition to the outlet. The way OpenFoam approximates ω allows it to be applied unconditionally of the y^+ value of the grid.

P_{rgh}

P_{rgh} is the reduced pressure. within OpenFoam the reduced pressure is defined as $P_{rgh} = p - \rho g h$ where h is the distance between the free-surface and the bottom of the domain. The fixedFlux boundary conditions imposes a zero gradient on the boundary. This gradient is formulated as follows, $\nabla P_{rgh} = \nabla P - \nabla \rho g h$ In the geometry used in this thesis fixedFlux boundary condition is imposed on the outlet and on the inlet. The outlet and inlet are parallel to the y-axis therefore the zero gradient boundary condition reduces to $\frac{\partial p_{rgh}}{\partial x} = \frac{\partial P}{\partial x} = 0$.

ν_t

In the k-OmegaSST model used in this thesis the turbulent viscosity is a function of k and ω. Since k and ω are prescribed, ν_t can be calculated from these values. OpenFoam needs this boundary file to be specified. For this reason all bc's except for the empty faces and the symmetry plane are calculated bc's.

k

The inlet kinetic turbulent intensity (k) is estimated by means of the following equation

$$k = 1.5 I^2 U^2 \tag{3.41}$$

Here I is the turbulent intensity of the mean flow which is estimated to be 0.02 Resulting in $k \approx 0.0015$. At the outlet we assume that the flow is identical to the inlet value, therefore the inletOutlet bc is used. In the vicinity of a wall there is an option to use a wall function or to adjust the first cell height below $y^+ = 1$. If a wall function is used, OpenFoam presents two options. One for low Reynolds number flow and one for turbulent flow. The latter was used in this thesis. It is called the kqRWallFunction and it imposes a zeroGradient boundary condition.

ψ
This value represents the volume fraction of water. To specify an inflow of water and air at the inlet prescribed values of ψ are used. At the outlet zero gradient is imposed. At walls the gradient should be zero as well. Values 1 and 0 are used for water and air respectively. A zeroGradient condition is specified at other boundaries.

Table 3.2: All boundary conditions in OpenFoam syntax that are applied for the given field values in the model

boundary	U	ω	P_{rgh}	ν_t	k	ψ
INLETAIR	*FixedValue*	*fixedValue*	*fixedFluxPressure*	*calculated*	*fixedValue*	*fixedValue*
INLETWATER	*FixedValue*	*fixedValue*	*fixedFluxPressure*	*calculated*	*fixedValue*	*fixedValue*
OUTLETAIR	*outletPhaseMeanVelocity*	*inletOutlet*	*fixedFluxPressure*	*calculated*	*inletOutlet*	*zeroGradient*
OUTLETWATER	*outletPhaseMeanVelocity*	*inletOutlet*	*fixedFluxPressure*	*calculated*	*inletOutlet*	*zeroGradient*
TOP	*symmetry*	*symmetry*	*symmetry*	*symmetry*	*symmetry*	*symmetry*
BOTTOM	*slip*	*omegaWallFunction*	*fixedFluxPressure*	*calculated*	*kqRWallFunction*	*zeroGradient*
AIRFOIL	*zeroGradient*	*omegaWallfunction*	*zeroGradient*	*nuWallFunction*	*fixedValuorkqRWallFunction*	*zeroGradient*
FRONTBACK	*empty*	*empty*	*empty*	*empty*	*empty*	*empty*

3.3. Damping of waves

A common source of numerical errors is wave reflection from the edges of the domain. To overcome this numerical phenomenon two solutions are discussed.

elongation of grid cells
A very effective way of damping waves towards the edges of the domain is by increasing the cell size in the direction of the flow. This procedure takes advantage of numerical diffusion

sponge layer
A sponge layer is a region close to the domain edge in which waves are dampened. figure 3.3 gives an impression of the way sponge layers are adapted in simulations with free surface waves.

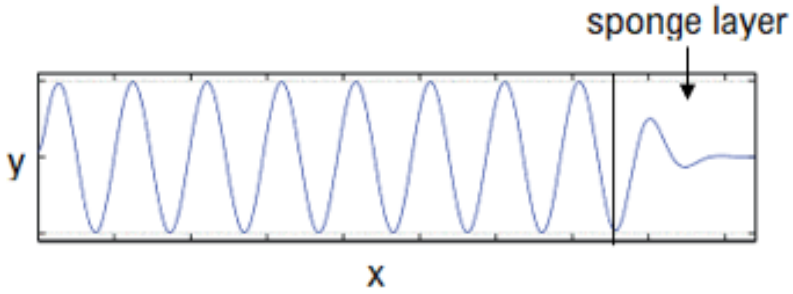

Figure 3.3: example of wave dampened with a sponge layer, The blue line represents a free-surface wave in the region named sponge layer the wave is dampened.

In OpenFoam the sponge layer is applied using the vertical damping fvOption. Here vertical damping is realized by applying a damping force proportional to the momentum of the flow in gravitational direction. (The OpenFOAM Foundation, 2019)

$$\frac{d(mu_y)}{dt} = -\lambda m u_y \tag{3.42}$$

$$u_y = u_{y0} e^{-\lambda t} \tag{3.43}$$

Here λ is the constant of proportionality, this value can be changed to increase the damping force. A discussion on the size and strength of the sponge layer is given in chapter 4 validation and results.

3.4. Initialisation

Small time steps are necessary to accurately simulate multiphase models. To reduce computation time the mesh is first ran using larger time steps. Initially a maximum Courant Friedrich Lewis number CFL is 0.25 and for the interface CFL_i 0.125. when initial start up behavior is gone the time steps are reduced by a factor 10. To identify whether non-physical flow behavior is completely eliminated the drag and lift are plotted against simulation time.

3.5. Convergence

Several quantities are monitored to check convergence. This section aims to elaborate on the convergence check procedure.

3.5.1. Residuals

First and foremost, the convergence of the simulation needs to be judged. This is done by checking the residuals of the numerical scheme. The residual is given as follows

$$\underline{\mathrm{R}}^n = \underline{\underline{A}} \cdot \underline{\varphi}^n - \underline{\mathrm{b}} \tag{3.44}$$

Here A is the coefficient matrix φ the solution vector and b is a vector of constants which is the right hand side of the linear algebraic system. The root mean squared (RMS) residuals are used to determine convergence. An RMS residual of $1 \cdot 10^{-4}$ is considered loosely converged, $1 \cdot 10^{-5}$ is considered well converged and if the value is $1 \cdot 10^{-6}$ or smaller, the solution is tightly converged. Kuron (2015)

3.5.2. lift and drag

For each case the mean of the lift coefficients is calculated together with the mean drag value. If the result is instationary , averaging is done over a number of fluctuations in the drag and lift values. Drag and lift coefficient C_l & C_d are calculated as follows.

$$C_\mathrm{l} = \frac{2F_\mathrm{y}}{\rho U^2 c} \tag{3.45}$$

$$C_\mathrm{d} = \frac{2F_\mathrm{x}}{\rho U^2 c} \tag{3.46}$$

The drag and lift coefficient are plotted against the run time, this is a very clear indicator of the convergence of the solution.

In conclusion this chapter provides the model set up, mathematical background and the procedure for assessment of convergence is described. The next chapter will cover the the background of the experiments from Duncan et al. (Duncan, 1983) that are used for validation. Also the results from other researchers that have worked on this problem is discussed.

4

Validation and Results

4.1. introduction

This thesis aims to model free surface waves, induced by a shallowly submerged naca0012 hydrofoil. In this chapter several methods are used to investigate whether the correct boundary conditions and turbulence parameters are used. Also the difficulties that come with free surface modeling in VOF is discussed. Several geometries are used.
Developed flow in a single phase channel is modeled. This is done to check the working of k-ωSST, and to check if the correct turbulence inflow parameters are used. After the developed channel has been investigated a single-phase airfoil test case is ran. This is done to check grid dependence of airfoil flows. The single phase airfoil case is also used to investigate the accuracy of the InterFoam package compared to the simpleFoam solver from openFoam. After these two tests the two phase flow from Duncan's experiment is modeled. The effect of grid quality for modeling airfoil flows is also discussed in this section. At the end of this chapter a breaking wave case is evaluated.

4.2. single phase channel

In this thesis several numerical studies are used to compare and draw conclusions from. Often the y^+ value is not documented. For the studies that provide the reader with the y^+ values, the values range between 0.5 and 10. In this section a discussion is given on the effect of the y^+ value on the resulting flow in a k$-\omega SST$ model.
A channel is made in which a fully developed flow is modeled. This is done using the cyclic boundary condition in openFoam. This boundary condition allows the user to specify two faces through which the flow is continuously recirculated. The result of this set-up is that we can simulate fully developed channel flow using only 1 or 2 grid cells in the flow direction. Figure 4.1 schematically represents the geometry with the cyclic boundaries. The flow is driven by an artificial pressure gradient called $\frac{dp}{dx}$. The value of $\frac{dp}{dx}$ and channel height are chosen such that the wall shear velocity (u_τ) equals 1. This is done because the results from Kim and Moin (Kim u. a., 1987) and Moser et al. (Moser u. a., 1999) are normalized with the friction velocity. The results from the fully developed channel are used to investigate how well K$-\omega$SST performs for different wall spacing and wall treatments.

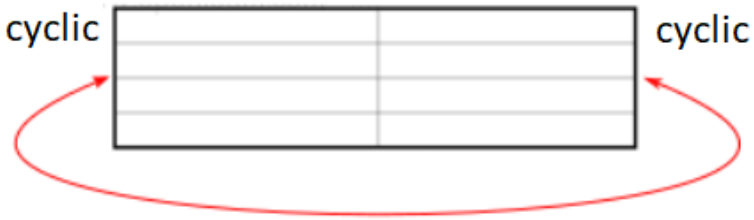

Figure 4.1: schematic representation of the model set-up for channel flow with a cyclic boundary field. the red arrow represents the recirculation of the resultant flow as input for the next cycle. The unnamed sides represent the walls of the channel.

Wall spacing is chosen such that $y^+ = 0.7$, 15 and 60. These y^+ values are chosen such that all sub regions (discussed in section 3.2.4) of the near wall region are represented.
The channel flow simulation is divided in 4 cases. The first to c1 and c2 correspond to $y^+ = 0.7$ and $y^+ = 15$ are ran with a fixed value for k, $k = 0$. The other two $y^+ = 15$ and 60 adopt the kqRWallfunction from openFoam. $y^+ = 15$ lies in the buffer layer, we want to know how the wallfunction from openFoam behaves for this y^+ value. Therefore both a wall function and a fixed value simulation are performed for $y^+ = 15$. Table 4.1 lists the basic input parameters for the cases. All cases are ran for $Re_{u_*} = 180$ and 590. $Re_{u_*} = \frac{u_* d}{\nu}$ based on friction velocity and channel half width. The results from Re = 590 are used to compare against a DNS performed by Moser et al. The results from $Re = 180$ are compared against Kim and Moin (Kim u. a., 1987).

Table 4.1: input parameters for the channel flow tests. 5 different setups are used in which the y^+ and k wall treatment is varied. These are names c1, c2,c3 and c4 respectively.

parameter	c1	c2	c3	c4
k	0	0	$kqRWallFunction$	$kqRWallFunction$
ω	$omegaWallFunction$	$omegaWallFunction$	$omegaWallFunction$	$omegaWallFunction$
g	2	2	2	2
h	1	1	1	1
y^+	0.7	15	15	60

The numerical schemes used for the channel cases are given below.

Table 4.2: Numerical schemes used in the cyclic channel cases

quad	Term	Discretization
Gradient	∇	Gauss linear
Convection	$\nabla \cdot (\rho \phi U)$	bounded Gauss linearUpwind grad(U)
	$\nabla \cdot (\phi k)$	Gauss upwind
	$\nabla \cdot (\phi \omega)$	Gauss upwind
	$\nabla \cdot ((\rho \nu_{Eff}) \cdot dev(\nabla U)^T)$	Gauss linear
Laplacian	∇^2	Gauss linear corrected

Convergence of turbulent channel flow is time consuming. To ensure that the flow is fully developed, the residuals are plotted against the number of iterations. If all residual values drop below $1 \cdot 10^{-6}$ the solution is considered converged. Kuron (2015)

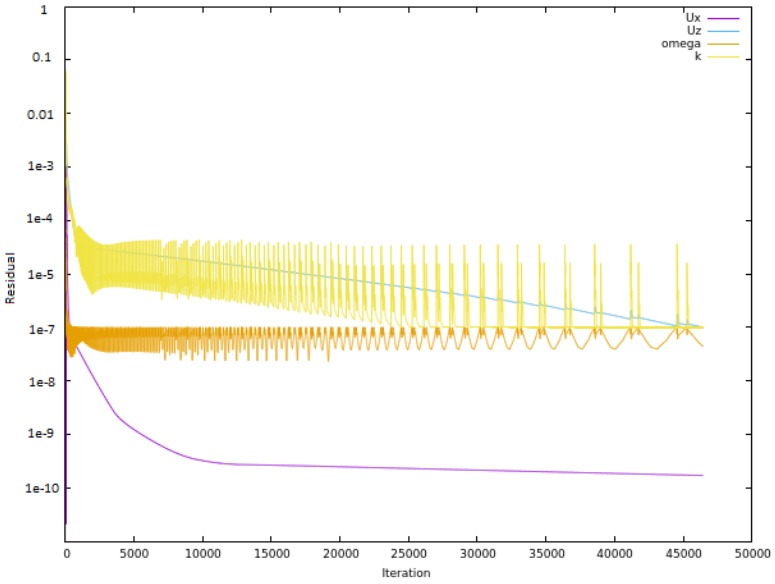

Figure 4.2: development of residuals for: u_x purple,u_z blue,ω orange,k yellow. Plotted against the number of iterations.

We want to compare the internal channel flow with external airfoil simulation. To compare these two flows we have to find a length scale that is present in both flows. The Reynolds number based on this length scale must be of the same order of magnitude. A length scale that is present in both flows is the boundary layer thickness (δ).

$$Re_\delta = \frac{U\delta}{\nu} \tag{4.1}$$

If Re_δ is of the same order of magnitude for the channel as for the multiphase airfoil case (presented in section 4.4.2) comparable turbulence is assumed. The boundary layer of a fully developed channel lies somewhere between $\frac{1}{10}$ and $\frac{1}{20}$ of the channel half width. At the airfoil the boundary layer increases over the length of the foil. The boundary layer reaches maximum thickness at the rear of the foil. At this point the thickness is approximately $\frac{1}{25}$ chord length (c). For both the external airfoil flow and the fully developed channel flow we want to rewrite the Reynolds number based on the mean flow in terms of Re_δ. For the high Reynolds channel flow $Re_m = 17500$. Re_m is the Reynolds number based on the center velocity. This results in $Re_\delta \approx 1750$. The airfoil case is ran at $Re_c = 2 \cdot 10^5$ based on the chord length. Resulting in $Re_\delta \approx 8000$. Re_δ from the comparison with Kim and Moin (Kim u. a., 1987) is approximately 330. This is orders of magnitude lower than the airfoil case. The results from this test case can be found in the appendix.

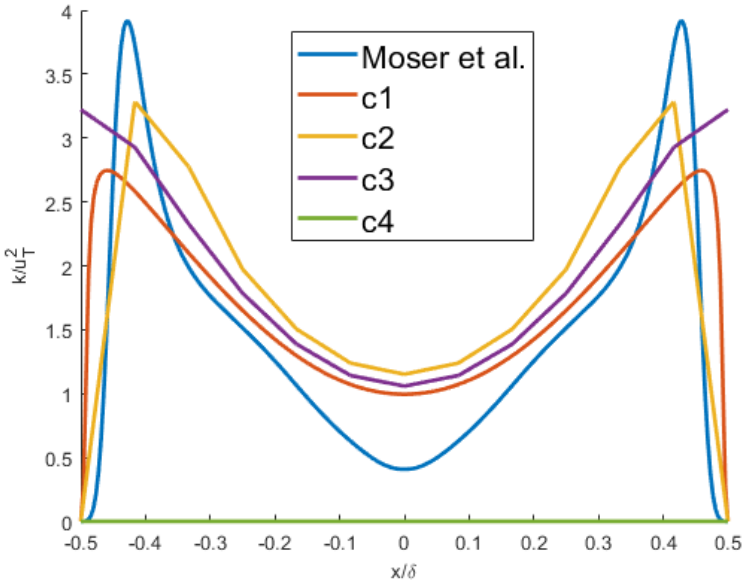

Figure 4.3: comparison of k between DNS performed by Moser (Moser u. a., 1999), and present study for $Re = 590$ blue: data from Moser etal. (Moser u. a., 1999) , red: c1, purple: c2, yellow: c3 green: c4. The green line at the bottom represents the simulation with $y^+ = 60$. This run did not converge because there where only 2 cells orthogonal to the flow direction. Corresponding y^+ values: c1:0.7, c2:15 ,c3:15 ,c4:60.

From figure 4.3 it is evident that near the wall values of k are underestimated. David.C. Wilcox compared the results from Moser et al. (Moser u. a., 1999) with the $k-\omega$ model (Wilcox u. a., 1998). He concludes that k$-\omega$ underestimates k in close proximity of the wall. The k$-\omega$SST turbulence model is identical to $k-\omega$ close to a wall. Underestimation of k is also found for c1 in the present study. c2 gives surprisingly good results.The peak region of k is not resolved which is clear by the straight line close to the wall. The wall function that was used in c3 fails to predict k and gives a wrong non zero value at the wall. Due to the large y^+ value not enough cells could be placed perpendicular to the wall. c3 did not converge due to this lack of cells and the result is therefore not reliable. Throughout the flow a very low value of k is given as a result for c3, but this is not physical. Wilcox (Wilcox u. a., 1998) concludes that even though k is not correctly modeled in this turbulence model the velocity profile is very accurate.
The velocity profiles for c1 up to c4 are plotted against the velocity profile from Moser et al. (Moser u. a., 1999).

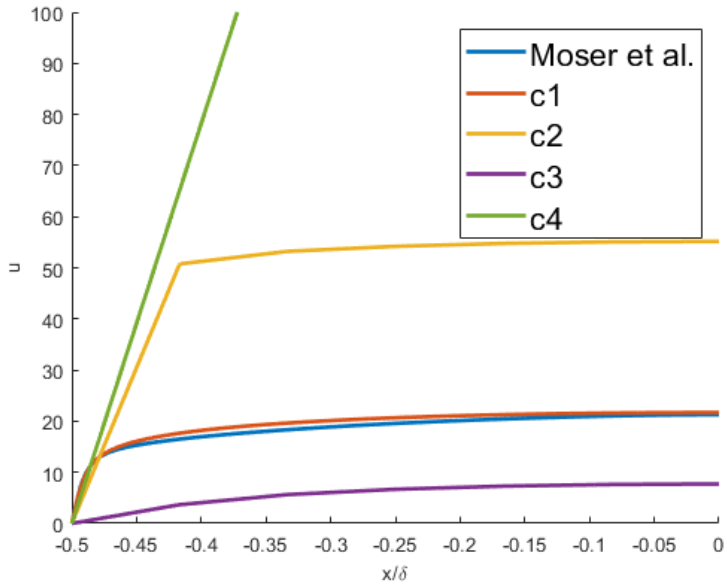

Figure 4.4: comparison of u between DNS performed by Moser (Moser u. a., 1999), and present study for $Re = 590$ blue: data from Moser etal. (Moser u. a., 1999) , red: c1, purple: c2, yellow: c3 green: c4. The velocity profile from C4 has not been plotted completely because it was orders of magnitude larger than to other results.

From figure 4.4 we see that the mean velocity is only accurately predicted by c1 ($k = 0, y^+ = 0.7$). C4 gave an extreme velocity profile which is the result of having only three cells orthogonal to the wall, with the first cells directly to the wall being outside the log region.
From this test case we can conclude that k$-\omega$SST is accurate enough to model the flow in the given Re regime. This only applies if grids are modeled such that k is fully resolved. Which corresponds to y^+ values below 1.

4.3. single phase airfoil

A study is performed on a naca0012 airfoil in a single fluid with $Re = 2 \cdot 10^5$ and an angle of attack of 5°. The airfoil, attack angle and Re are chosen to match the setup from Duncan's experiment (Duncan, 1983). This case study is used as a basis for the more complex two phase simulation later in this thesis. Single phase flow over an airfoil is relevant for the aviation industry, wind energy sector among other industries. This broad field of application results in significantly more data for airfoil flows at $Re = 2 \cdot 10^5$ than in multiphase situations. This data is used to validate the current model. Another advantage of single phase simulation is the reduced computation time. Multiple grids are generated to check accuracy of the model. Convergence is analyzed by means of the residuum and lift and drag coefficients.
Modeling single phase flow turned out to be more difficult than expected. This came about when results were compared against panel vortex methods (Hepperle, 2019). The hypothesis is that transition of the boundary layer regime is not correctly modeled.

Table 4.3: Generated meshes for the C-type grids: m1,m2 and m3. m4 is the mesh used in the multiphase model.

Mesh	α °	wall spacing (c)	growth factor	faces on hydrofoil	total number of cells $\cdot 10^4$
$m1$	5	0.0036	1.2	97	0.96
$m2$	5	0.0036	1.1	177	2.7
$m3$	5	0.0036	1.1	257	3.9
$m4$	5	0.001	1.05	494	27.6

For this test case three c-type grids are made, figure 4.5. global parameters are listed in table 4.3 (m1,m2.m3). An example of the grid is given in the appendix. In addition to those grids the mesh used in the multiphase model is also ran in single phase in this section, it is referred to as m4. Five cases are evaluated from the aforementioned grids. m1, m2 and m3 are ran with the simpleFoam solver these simulations are denoted

s1,s2 and s3 respectively. This is done to show grid convergence. Using interFoam both m3 and m4 are evaluated those two simulations are further referred to as s4 and s5 respectively. Table 4.4 lists the set up for the five cases denoted s1 up to s5.

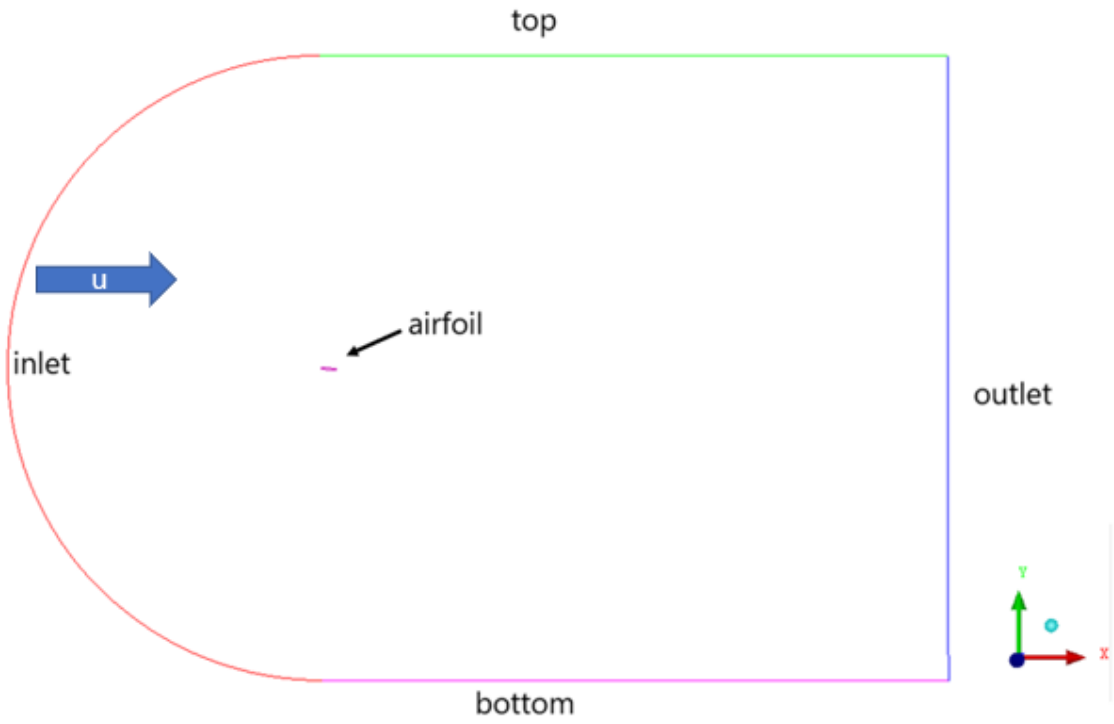

Figure 4.5: geometry used in the singlephase test cases

Table 4.4: input parameters for the single phase tests. 5 different setups are used in which the grid and solver is varied. These are named s1, s2,s3, s4 and s5 respectively.

parameter	s1	s2	s3	s4	s5
mesh	*m*1	*m*2	*m*3	*m*3	*m*4
solver	*simpleFoam*	*simpleFoam*	*simpleFoam*	*interFoam*	*interFoam*
residual control	$1e-10$	$1e-10$	$1e-10$	$1e-10$	$1e-10$
k *at foil*	0	0	0	0	0
k *inlet*	0.0015	0.0015	0.0015	0.0015	0.0015
ω *at foil*	*omegaWallFunction*	*omegaWallFunction*	*omegaWallFunction*	*omegaWallFunction*	*omegaWallFunction*
ω *inlet*	0.1	0.1	0.1	0.1	0.1

Table 4.5: Numerical schemes used for cases s1, s2 and s3

quad	Term	Discretization
Gradient	∇	Gauss linear
Convection	$\nabla \cdot (\phi U)$	Gauss limitedLinearV 1
	$\nabla \cdot ((\nu_{Eff}) \cdot dev(\nabla U)^T)$	Gauss Linear
	$\nabla \cdot (\phi \omega)$	bounded Gauss upwind
	$\nabla \cdot (\phi k)$	bounded Gauss upwind
Laplacian	∇^2	Gauss linear corrected

Table 4.6: Numerical schemes used for cases s4 and s5

quad	Term	Discretization
Gradient	∇	Gauss linear
Convection	$\nabla \cdot (\rho\phi U)$	Gauss limitedLinearV 1
	$\nabla \cdot (\phi\alpha)$	Gauss vanLeer01
	$\nabla \cdot (\phi_{rb}\alpha)$	Gauss interfaceCompression
	$\nabla \cdot ((\rho\nu_{Eff}) \cdot dev(\nabla U)^T)$	Gauss Linear
	$\nabla \cdot (\phi\omega)$	bounded Gauss upwind
	$\nabla \cdot (\phi k)$	bounded Gauss upwind
Laplacian	∇^2	Gauss linear corrected

The aformentioned simulations are compared against the result generated in Javafoil. JavaFoil is an open-source panel method that allows simple airfoil flows to be simulated. The vortex panel method that is adopted by JavaFoil is based on potential flow analysis. The program allows the user to chose several boundary layer methods. The boundary layer method uses the velocity distribution to calculate the viscous boundary layer. These calculations are based on the formulas presented by Eppler (Eppler, 1963, 1978, Eppler und Somers, 1980). On the website a Reynold regime of $5 \cdot 10^5 \leq Re \geq 2 \cdot 10^7$ is adviced. The tranition methods by Eppler are recommended for flows above $Re = 1 \cdot 10^5$.

For the 5 setups given in table 4.4 the pressure coefficient (Cp) is plotted at the airfoil.

$$Cp = \frac{p - p_0}{\frac{1}{2}\rho U^2} \tag{4.2}$$

The results from s1,s2 and s3 are compared against the pressure coefficient from Javafoil (Hepperle, 2019). This is done to identify how grid refinement effects the resulting pressure profile at the airfoil. The results are given in figure 4.6. Increase in the number of nodes near the stagnation point does not significantly change the result. In contrast, refinement at the rear of the foil does increase the accuracy of the model, this can be seen by the red squares in figure 4.6. The pressure coefficient is underestimated near the stagnation point in all cases.

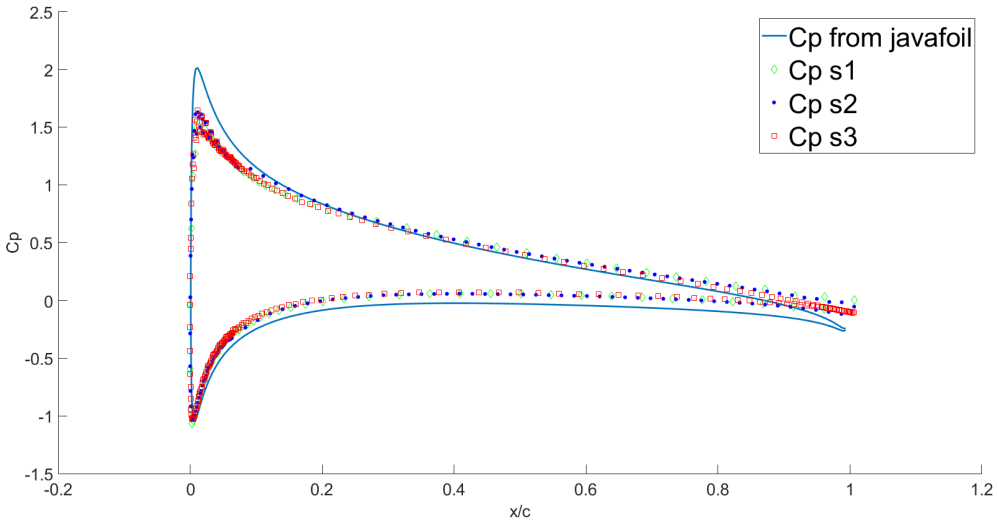

Figure 4.6: Pressure coefficient for a naca0012 airfoil in single phase. s1,s2 and s3. Compared to the pressure coefficient generated in javafoil (Hepperle, 2019).

The difference between the result from the simpleFoam and interFoam solver for the same grid is shown in figure 4.7.

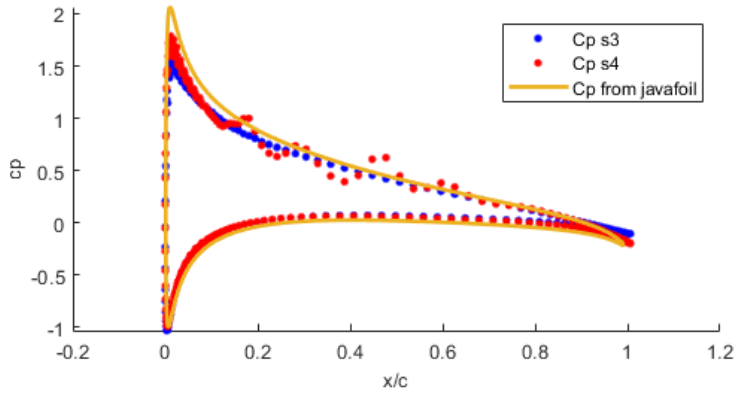

Figure 4.7: Pressure coefficient for a naca0012 airfoil in single phase. s3 and s4 which are simulations on the same grid. s3 is solved with simpleFoam and s4 at with interFoam $t = 84$. Compared to the pressure coefficient generated in javafoil (Hepperle, 2019). Wiggles in the result from s4 suggest separation of the boundary layer.

From figure 4.7 we see that the interFoam solver results in a closer fit to the pressure coefficient from Javafoil. There is still an underestimation of the pressure coefficient near the stagnation point.
The pressure coefficient from s5 is compared with the result form the refined c-type grid that was also solved with the interFoam solver. Javafoil (Hepperle, 2019). Extra refinement at the rear results in a good fit. The underestimation of the pressure coefficient near the stagnation point is also found in this case.

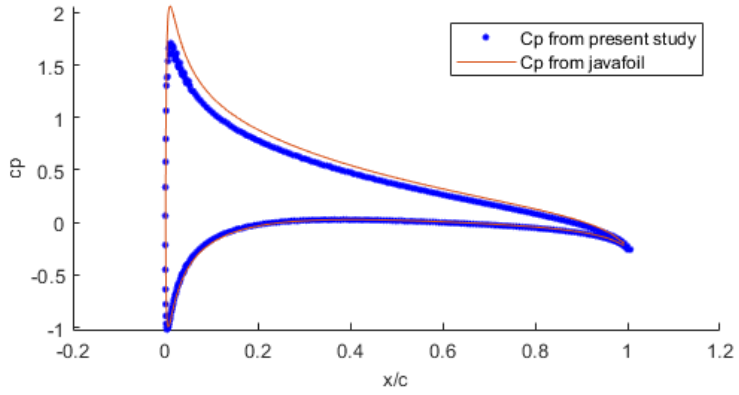

Figure 4.8: Pressure coefficient from s5. Compared to the pressure coefficient generated in javafoil (Hepperle, 2019).

The difference between the vortex panel method from Javafoil and the present study raises questions about

the accuracy of both methods. To further investigate this the results from Yousefi et al. (Yousefi und Razeghi, 2018) and Aktharuzzaman and his colleagues (Md Aktharuzzaman, 2012) are used. The model setup for all studies are listed in table 4.7. The dash sign (−) is used when there is no data available from the source or if it is not applicable for that model.

Table 4.7: Summary of models used for Drag and lift comparison on single phase naca0012 foil

source	Re $\cdot 10^5$	α	solver	program	nodes on foil	y^+
$javafoil$	2	5	vortex panel method	javafoil	180	–
$Yousefi$	5	5	vortex panel method	Fortran	180	–
$AktharuzzamanAnsys$	2	6	k−ω SST	Ansys Fluent	–	1
$Aktharuzzamanexp$	2	6	experiment	–	–	–

Comparison of all studies is done by means of the lift and drag of the airfoil. They are listed in table 4.8. In the appendix an example of the convergence of lift and drag coefficients for the c-type grid is given.

Table 4.8: Comparison of lift and drag at the hydrofoil generated by OpenFoam javaFoil (Hepperle, 2019) results from Yousefi and Razeghi (Yousefi und Razeghi, 2018) and data from the experiment by Aktharuzzaman et al.(Md Aktharuzzaman, 2012)

Mesh	Re $\cdot 10^5$	α	Cl	Cd
$s3$	2	5	0.49	0.016
$s4$	2	5	0.62	0.010
$s5$	2	5	0.57	0.02
$javafoil$	2	5	0.59	0.017
$Yousefi$	5	5	0.63	0.010
$Aktharuzzaman$	2	6	0.66	0.04

The Reynolds regime in which this single phase test case was performed could be the reason for differences in the results given in table 4.8. For $Re = 2 \cdot 10^5$ and an angle of attack of 5% the boundary layer transitions from laminar to turbulent at approximately $0.3\frac{x}{c}$ (Yousefi und Razeghi, 2018). The RANS model $k-\omega$ is known to show premature transition of the boundary layer (Wilcox u. a., 1998). Figure 4.9 depicts a plot of the wall shear stress at the airfoil for case s3. A hump in the Cp for the top part of the hydrofoil is clear. This indicates that transition occurs at $\frac{x}{c} \approx 0.1$. Turbulent boundary layer generate more skin friction which in case of a slender body accounts for the majority of the total friction. (White u. a., 2011)

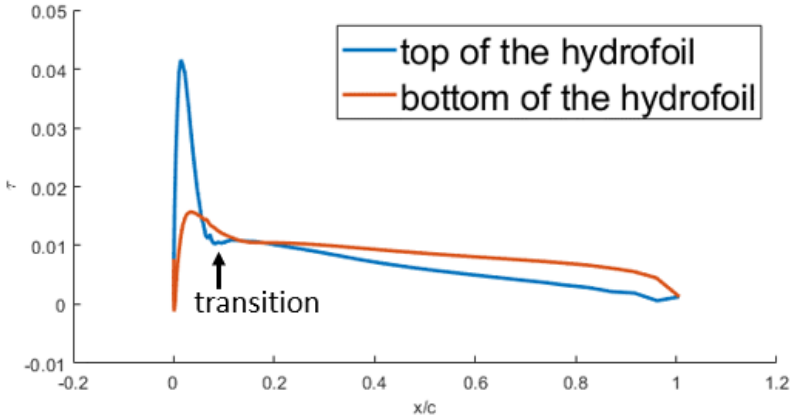

Figure 4.9: Wallshear stress τ at the airfoil, data from s3. Red: bottom of the hydrofoil, blue: top of the hydrofoil. Note that the hump in the blue line at $\frac{x}{c} = 0.1$ indicates the start of transition from laminar to turbulent boundary layer regime.

4.4. multiphase model

4.4.1. grid study

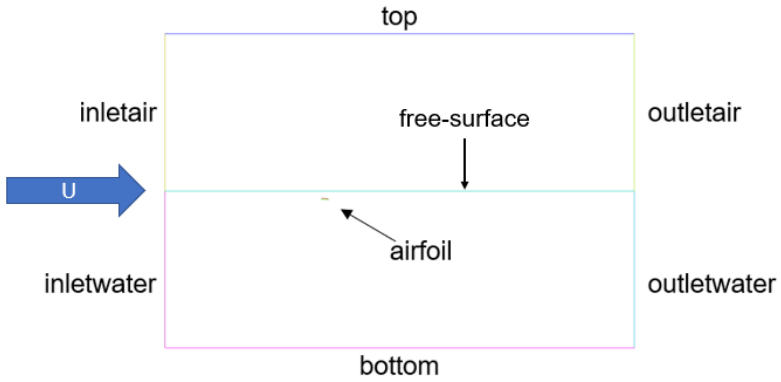

Figure 4.10: geometry used for multiphase modeling. The blue arrow indicates the flow direction. The thin blue line in the middle of the geometry represents the free-surface in the undisturbed situation.

In advance of the multiphase analysis a grid dependency study is carried out. A grid study is performed for two reasons. The first is that we want to be sure that the grid does not significantly effect the resulting flow that we want to model. The second reason is that it is desirable to have a grid which is as coarse as possible, while still accurately representing the desired flow. Such a coarse grid is desired since this can have a major impact on simulation time.
The grid study is done by creating six different meshes on the same domain. The domain from the experiments performed by Duncan et al. (Duncan, 1983) is used. In section 2.2 this geometry is explained. All meshes are ran with the same numerical setup. The boundary conditions that are used are listed in table 4.9. The numerical schemes are given in table 4.10.

Table 4.9: For all grids the turbulence kinetic energy was fixed at the wall with a value of 1e-18. This small value is used to prevent the model from a mathematical crash due to division by 0.

boundary	U	ω	P_{rgh}	ν_t	k	ψ
INLETAIR	(1.775600)	0.1	$fixedFluxPressure$	$calculated$	0.0015	$fixedValue$
INLETWATER	(1.775600)	0.1	$fixedFluxPressure$	$calculated$	0.0015	$fixedValue$
OUTLETAIR	$outletPhaseMeanVelocity$	0.1	$fixedFluxPressure$	$calculated$	0.0015	$zeroGradient$
OUTLETWATER	$outletPhaseMeanVelocity$	0.1	$fixedFluxPressure$	$calculated$	0.0015	$zeroGradient$
TOP	$symmetry$	$symmetry$	$symmetry$	$symmetry$	$symmetry$	$symmetry$
BOTTOM	$slip$	$omegaWallFunction$	$fixedFluxPressure$	$calculated$	$kqRWallFunction$	$zeroGradient$
AIRFOIL	$zeroGradient$	$omegaWallfunction$	$zeroGradient$	$nutWallFunction$	$1e-18$	$zeroGradient$
FRONTBACK	$empty$	$empty$	$empty$	$empty$	$empty$	$empty$

Table 4.10: Numerical schemes used in this thesis

quad	Term	Discretization
Gradient	∇	Gauss linear
Convection	$\nabla\cdot(\rho\phi U)$	Gauss limitedLinearV 1
	$\nabla\cdot(\phi\alpha)$	Gauss vanLeer01
	$\nabla\cdot(\phi_{rb}\alpha)$	Gauss interfaceCompression
	$\nabla\cdot((\rho\nu_{Eff})\cdot dev(\nabla U)^T)$	Gauss linear
	$\nabla\cdot(\phi\omega)$	bounded Gauss upwind
	$\nabla\cdot(\phi k)$	bounded Gauss upwind
Laplacian	∇^2	Gauss linear corrected

The six grids are gradually refined with 11 being the coarsest grid and 16 the most refined one. Table 4.11 lists the important parameters of the grids. Wall spacing denoted in the third column is the height of the first cell adjacent to the hydrofoil. There are three values used for the wall spacing. These are 0.0036c ,0.001c and 0.0001c. The largest wall spacing 0.0036c has been chosen such that the resulting y^+ value is below 5, which is the advised value for modeling within the laminar sub-layer discussed in section 3.2.4. The second is chosen such that the maximum of $y^+ \approx 0.7$ this was the value that resulted from the developed turbulent channel test case in section 4.2. The last wall spacing (0.0001c) was chosen to investigate if extra refinement close to the wall has an effect on the results.

Table 4.11: Generated meshes for *case*1 identical to the setup from Duncan et al. (Duncan, 1983)

. Wall spacing is the height of the first cell at the hydrofoil and at the bottom. The cells at the interface are approximately square in the region of interest, therefore only one length is given.

Mesh	α °	h	wall spacing (m)	growth factor	total number of cells $\cdot 10^4$	faces on hydrofoil	cell size at interface
11	5	0.955	0.0036	1.4	4.7	267	0.02
12	5	0.955	0.0036	1.3	6.7	447	0.01
13	5	0.955	0.0036	1.2	8.1	484	0.01
14	5	0.955	0.001	1.1	8.7	494	0.01
15	5	0.955	0.001	1.05	13.7	475	0.01
16	5	0.955	0.0001	1.05	27.6	467	0.005

In table 4.11 the wall spacing is given. The height of the first cell is estimated to result in a desired y^+ value. For each simulation y^+ is calculated at the hydrofoil. the minimum, maximum and average values for y^+ are listed in table 4.12.

Table 4.12: Y^+ values over the surface of the hydrofoil, for each grid used in the grid study.

Mesh	min	max	average
11	0.68	9.2	3.0
12	0.65	8.6	3.9
13	0.22	2.8	0.90
14	0.052	0.67	0.15
15	0.049	0.66	0.17
16	$3.8e-3$	$3.2e-2$	$7.3e-3$

From table 4.12 we see that for grids 11,12 and 13 , the desired value of $y^+ \leq 5$ is satisfied. For grid 11 and 12 the maximum value lies in the buffer layer, this might have an effect on the results. This is further discussed below. The other three grids 14, 15 and 16 all meet the desired y^+ value of 0.7. Grids 14,15 and 16 are therefore expected to be able to model the boundary layer correctly. To further evaluate the grids, convergence of the simulations is analyzed by means of the residuals and drag and lift coefficients.

The residuals are used as an initial check for the convergence of the simulations. As described in section 3.5.1 a minimum value of $1e^{-6}$ is desired to consider the model converged. Residuals of the six grids are given in table 4.13.

Table 4.13: Residuals for meshes used in this grid study listed in table 4.11

Mesh	U_x	U_y	p_{rgh}	ω	k
11	$1.4 \cdot 10^{-7}$	$1.1 \cdot 10^{-12}$	$8.0 \cdot 10^{-8}$	$9.7 \cdot 10^{-8}$	$1.9 \cdot 10^{-7}$
12	$2.9 \cdot 10^{-7}$	$8.1 \cdot 10^{-13}$	$1.5 \cdot 10^{-8}$	$1.0 \cdot 10^{-8}$	$2.9 \cdot 10^{-7}$
13	$2.8 \cdot 10^{-10}$	$3.8 \cdot 10^{-9}$	$6.0 \cdot 10^{-8}$	$9.4 \cdot 10^{-7}$	$7.3 \cdot 10^{-10}$
14	$4.6 \cdot 10^{-13}$	$4.9 \cdot 10^{-12}$	$8.7 \cdot 10^{-8}$	$4.2 \cdot 10^{-8}$	$1.5 \cdot 10^{-7}$
15	$6.7 \cdot 10^{-10}$	$2.9 \cdot 10^{-9}$	$9.3 \cdot 10^{-8}$	$4.9 \cdot 10^{-7}$	$2.9 \cdot 10^{-11}$
16	$9.6 \cdot 10^{-11}$	$1.0 \cdot 10^{-9}$	$9.3 \cdot 10^{-8}$	$1.8 \cdot 10^{-7}$	$4.5 \cdot 10^{-7}$

At this point we know that all meshes converged based on the residuals. Also the wall spacing resulted in desirable values of y^+ except for grids 11 and 12. To qualitatively compare the results from the 6 grids, the lift and drag coefficient (Cl, Cd) are compared. Before we compare the results aforementioned coefficients are plotted against the simulation time. This is done because these plots clearly show the convergence of the simulation. Figure 4.11a and 4.11b are shown to give an impression of the convergence of these grids.

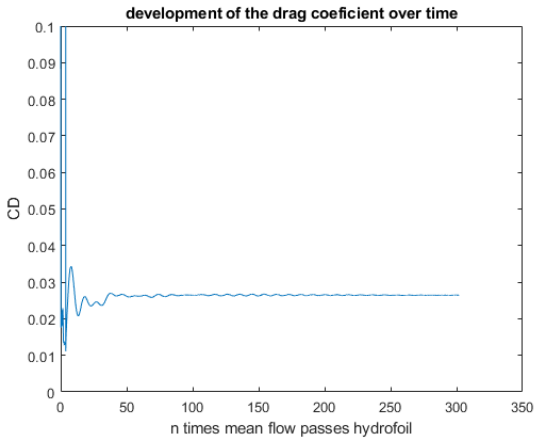

(a) development of the lift coefficient

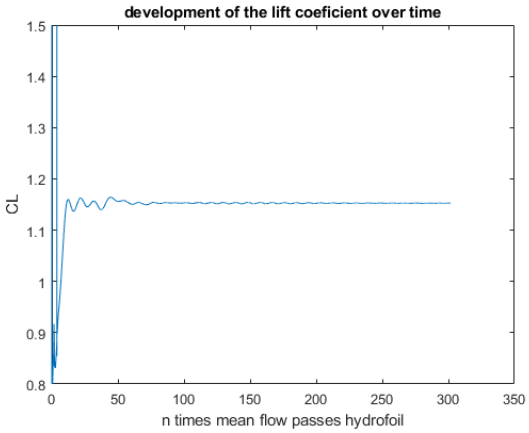

(b) development of the drag coefficient

Figure 4.11: lift and drag versus number of hydrofoil passings calculated from the mean flow velocity. Plot is made with the results from mesh 13. Convergence for both lift and drag is visible. Both plots show a slight oscillating result, which indicates that the flow is not steady state.

In the plots from figure 4.11 we can see that after an initial transient the converged coefficients show a periodic variation. In order to compare the results from these grids we want to find a single value for both coefficients. This is done by taking the mean value of the last three waves from the lift and drag coefficient results. The results are given in table 4.14.

Table 4.14: lift and drag at the hydrofoil from $case1$. Identical to the setup from Duncan et al. (Duncan, 1983)

Mesh	$C_{l,mean}$	$C_d, mean$
11	1.1	0.032
12	1.2	0.035
13	1.17	0.026
14	1.00	0.019
15	1.01	0.017
16	1.00	0.017

From table 4.14 we see that between grid 13 and 14 a big change is found in the drag and lift coefficients. The reason for this difference in the data is found to be that the coarser grids 11,12 and 13 show a breaking wave which is not expected from the results of Duncan's experiment. The reason for this breaking behavior might be related to the y^+ values. For the three finer grids we find a comparable outcome among one another, where between 14 and 15 a small difference is still present. Between grid 15 and 16 the results are almost identical and therefore we accept grid 15 to be fine enough to simulate the experiment performed by Duncan et al.
Duncan et al. (Duncan, 1983) provides a simple approach to calculate the wave making drag associated with a submerged hydrofoil for non-breaking waves. They assume that the drag from the hydrofoil is very small. By making this assumption they associate the total drag from their experiment to wave making drag. If we now look back at the results from the single phase foil case we see that the drag in that situation is of the same order of magnitude as in the multiphase case. The Cd values for both the single and mutliphase case are given in table 4.15

Table 4.15: drag at the hydrofoil from single phase test case compared to the result form the multiphase test case.

$C_{d,single}$	$C_{d,multi}$
$0.01-0.02$	0.017

Since both simulations have a drag of comparable magnitude we expect that the assumption of negligible drag made by Duncan and his colleagues was not valid.
In this thesis some geometrical parameters like submergence depth and basin depth are altered. Since these changes do not significantly change the expected flow profile we take the same grid parameters as used for grid 15 to create the other grids. No other grid studies will be performed on the new grids. It is important to note that grid 15 is the same grid that was denoted $m4$ in the single phase airfoil section 4.3.

4.4.2. multiphase non-breaking

In this section the numerical approximation of a non-breaking wave profile is discussed. An example of a non breaking wave profile is depicted in 5.5a. In the paragraph: Effect of grid and domain size, the sensitivity of the free surface profile to different grid parameters is discussed. In the paragraph, Floor effect, the assumption from Duncan et al. (Duncan, 1983) of being able to consider waves as deep water waves is evaluated. After the Floor effects a paragraph on the Reynolds effect for $2 \cdot 10^4 \geq Re \leq 2 \cdot 10^6$ is given. This paragraph reviews the Reynolds dependency of the free surface waves. Thereafter a subsection named Amplitude and wavelength. the subsection amplitude and wavelength, provides the reader with an analysis on which relevant parameters dominate the wave profile. The multiphase non-breaking section is finalized with the results from Chen and Chwang (Chen, 2012).

Effect of grid and domain size The free surface in VOF models is very sensitive to grid and domain size. In this section some of the effects and the solution by a variation of these parameters is discussed. An example of a wave profile as we would like to model it is given in figure 4.12

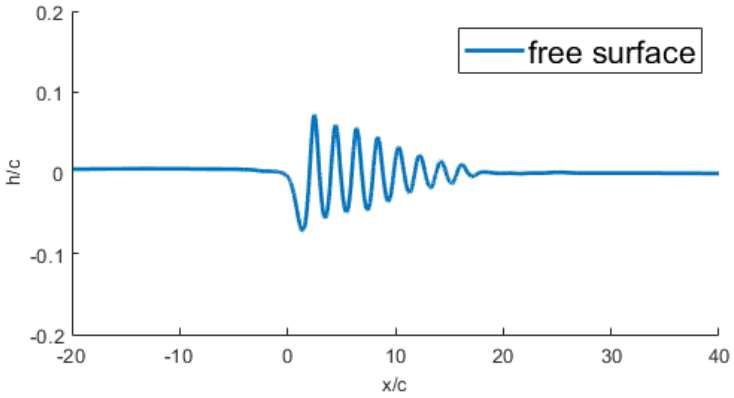

Figure 4.12: Example of a wave profile without unwanted grid effects. Note that the center of the hydrofoil is located at $\frac{x}{c} = 0$.

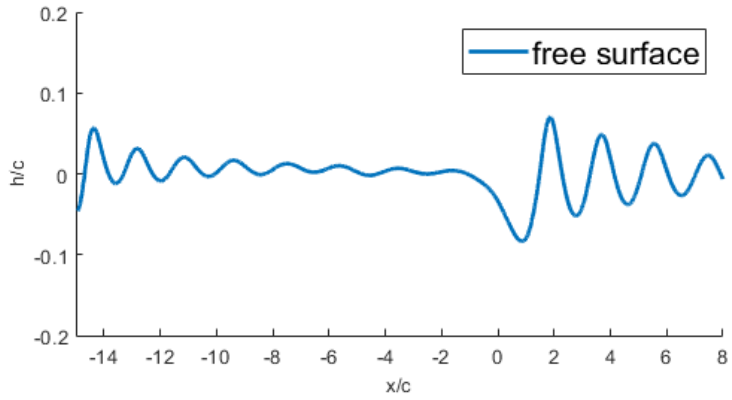

Figure 4.13: Wave profile that results from start-up without damping at the inlet

Figure 4.13 is a plot of the free surface with the inlet at 15c in front of the hydrofoil, without a sponge layer at the inlet. On start up of the simulation waves are generated at the hydrofoil. Waves propagate upstream and downstream. The waves moving towards the inlet accumulate and form a stationary wave profile. This wave profile does effect the wave train that is of interest. If the distance between the inlet and the hydrofoil is decreased, the free-surface elevation in the region of interest increases. Damping of the standing wave at the inlet can be realized by increasing the cell size gradually in the upstream direction. This increases numerical diffusion which smears out the waves. Another possibility is adopting a sponge layer. A sponge layer locally counters the vertical momentum of the wave profile. Damping methods are discussed in section: Damping of waves 3.3.

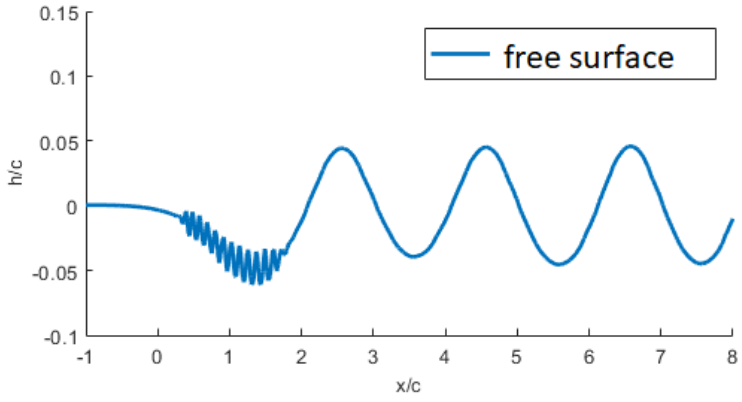

Figure 4.14: Wave profile that results from start-up with large aspect ratio between neighboring cells

Figure 4.14 depicts a nonphysical wave profile with a much smaller wavelength than the one produced by the hydrofoil. These waves are generated between two adjacent cells for which the aspect ratio is too large. The

free-surface in this model showed to be very sensitive to this effect. Even if the aspect ratio was only 1.1 the free surface started showing small disturbances in the form of waves with a small wavelength. This limitation in aspect ratio between neighboring cells conflicts with the increase in cell size to stimulate numerical diffusion as discussed is section: Damping of waves 3.3. An option to overcome this problem is increasing the domain size towards the inlet or adopt a sponge layer. When a sponge layer is used it is important that damping is done gradually to prevent reflection of waves from the sponge layer. The damping strength of a sponge layer is adjusted by changing the value of λ is this study a value of 0.1 is used. $\lambda = 0.1$ dampens a wave in approximately 10 wavelengths. In combination with the gradual increase of cell size with an aspect ratio of 1.05, this results in complete damping of waves within 20 chord lengths upstream and 40 chord lengths downstream. As a result of the aforementioned limitations of grid size and damping options, the following grid dimensions are chosen in the present study. A frontal domain size of 20 chord lengths of which the first five chord lengths are supplied with a sponge layer. Behind the airfoil the domain stretches 40 chord lengths. The last 10 chord lengths are supplied with a sponge layer.

Floor effect Chen and Wang (Chen, 2012), Walker et al.(Walker u. a., 2004), Di Mascio et al. (Di Mascio u. a., 2007) and Prasad et al. (Prasad u. a., 2015) all neglect the presence of the floor in Duncan's experimental setup. As mentioned before, Duncan does mention the effect of the floor on the lift of the hydrofoil. If the lift is increased by the presence of a floor, this effect might increase the amplitude of the wave profile. This could be an explanation for the general underestimation of the wave height in numerical simulations.
To evaluate whether the assumption of deep water regime is valid, the wavelength of the first trailing wave (λ_{t2}) and total water depth (D) from the experiments from Duncan are evaluated in table 4.16. If $\frac{D}{\lambda_{t2}} > 0.5$ deep water waves can be assumed (White u. a., 2011).

Table 4.16: $\frac{d}{\lambda}$ for experiments from Duncan et al (Duncan, 1983). Values for submergence 0.78 are missing because heavy breaking does not allow for wave length measurement

foil submergence $\frac{h}{c}$	total water depth $\frac{D}{c}$	wavelength second trailing wave $\frac{\lambda_{t2}}{c}$	$\frac{D}{\lambda_{t2}}$
1.29	2.2	2.1	1.0
1.16	2.0	2.1	0.95
1.03	1.9	2.0	0.95
0.95	1.8	1.9	0.95
0.95	1.8	1.9	0.95
0.91	1.8	1.9	0.95
0.78	1.7	–	–

From tabel 4.16 we see that $\frac{D}{\lambda_{t2}} \approx 1$ and this tells us that wave dynamics are not significantly effected by the presence of the floor in Duncan's experiments. The flow near the hydrofoil might still be influenced by the floor. Since the waves are generated by the flow over the hydrofoil further investigation is necessary.
Two different geometries are tested, the first (case1) is in accordance to the lab test set-up from Duncan et al. (Duncan, 1983). The second geometry (case2)is a submerged hydrofoil with the same level of submergence but with the bottom wall far away from the hydrofoil.
The geometry is modeled as depicted in figures 4.15. Height and length of the geometry are non-dimensionalized with the chord length c. Table 4.17 shows the geometrical parameters of each case. Submergence is varied in this thesis the attack angle is kept constant.

Table 4.17: Geometrical parameters of the cases evaluated in this thesis.

case	$\frac{x}{c}$ range	$\frac{y}{c}$ range	$\frac{h}{c}$	α
case1	$-20 \quad 40$	$-1.7692 \quad 20$	0.955	5°
case2	$-20 \quad 40$	$-20 \quad 20$	0.955	5°

Table 4.18 gives the basic parameters for the two cases that are compared in this section. Case1 is modeled after the experimental setup from Duncan et al. (Duncan, 1983) with the floor at 0.86c below the hydrofoil. Case2 is the same geometry except for the floor which is placed much further down, namely 10c below the

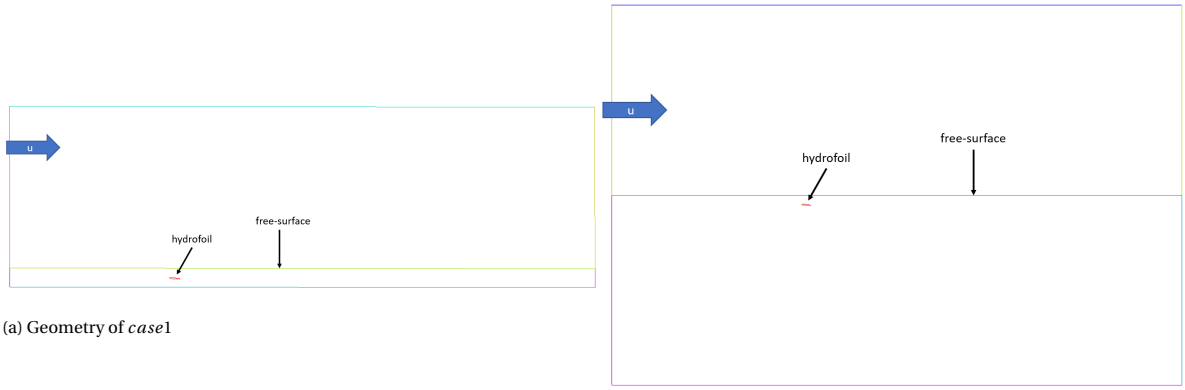

(a) Geometry of $case1$

(b) geometry of $case2$

Figure 4.15: geometry of the domains used in the present thesis. a: is equivalent to the experimental setup from Duncan et al. (Duncan, 1983). b differs from a in the distance between hydrofoil and the bottom of the domain. Note that in this thesis the free-surface is moved in vertical position, to simulate different levels of submergence.

free surface. Figure 4.16 depicts the wave profiles from case1 and case2 together with the experimental result

Table 4.18: Geometrical parameters of the cases evaluated for non-breaking conditions.

case	$\frac{x}{c}$ range	$\frac{y}{c}$ range	$\frac{h}{c}$	α
case1	$-20 \quad 40$	$-1.7692 \quad 20$	0.955	5°
case2	$-20 \quad 40$	$-20 \quad 20$	0.955	5°

from Duncan et al. (Duncan, 1983).

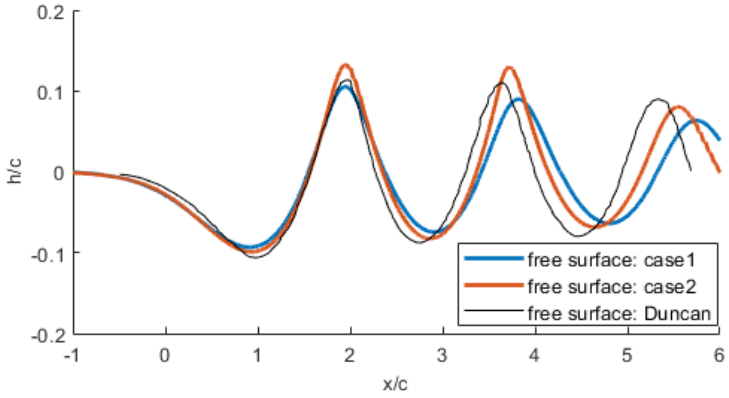

Figure 4.16: first three waves of the wave-profile generated by the submerged hydrofoil. The blue line is the present result with the same geometry as Duncan et al. ($Re = 2 \cdot 10^5$). The red Line is the wave profile with the bottom wall modeled at 10c below the hydrofoil ($Re = 2 \cdot 10^5$).

From figure 4.16 we can see that the floor positioned close to the hydrofoil results in an overall decrease of wave height, and a increase in wave length. If we look at the results from Duncan et al. (Duncan, 1983) the first wave is fairly accurately modeled by case1 with the floor at 10c below the hydrofoil. For the trailing waves

we see that the wave height lies somewhere between both results from the present study. The wavelength is shorter in Duncan's result than for both cases in the present study. Prasad et al. who used the k_ε RANS model also found an overestimation of the wave profile. From This analysis we can conclude that the Froude number based on the basin depth Fr_D is relevant for shallow submerged hydrofoil flows.

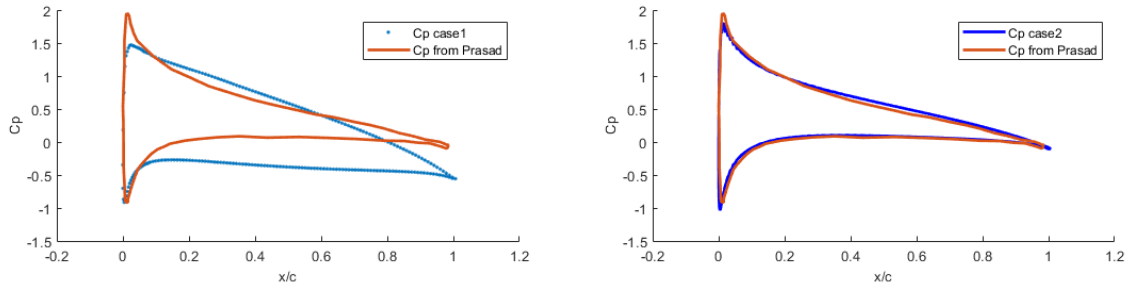

(a) pressure coefficient at the airfoil.
Blue represents the result case2 with the floor at 10c below the hydrofoil. Red is the result from Prasad et al. (Prasad u. a., 2015).

(b) pressure coefficient at the hydrofoil. Blue represents the result from the present study case1 with the floor at 0.86c below the hydrofoil. Red is the result from Prasad et al (Prasad u. a., 2015).

Figure 4.17: Pressure coefficient with and without floor effect.

To identify the effect the floor has on the flow over the hydrofoil, the pressure coefficient is plotted in figure 4.17 a and b. Both plots also show the pressure coefficient from Prasad et al. (Prasad u. a., 2015). The pressure distribution shows that the lift significantly decreased if a floor is close to the hydrofoil. The similarity in pressure coefficient from Prasad (Prasad u. a., 2015) and the present study case2 (where the floor is positioned at 10c below the hydrofoil, shows that Prasad did model with a floor far from the hydrofoil. For case1 in which the floor is positioned at 0.86c below the hydrofoil $Cl = 0.78$, case2 with the floor at 10c below the hydrofoil $Cl = 1.17$. The presence of the floor might also effect the boundary layer development on the hydrofoil. To investigate this the wall shear stress is plotted in figure 4.18 a and b.

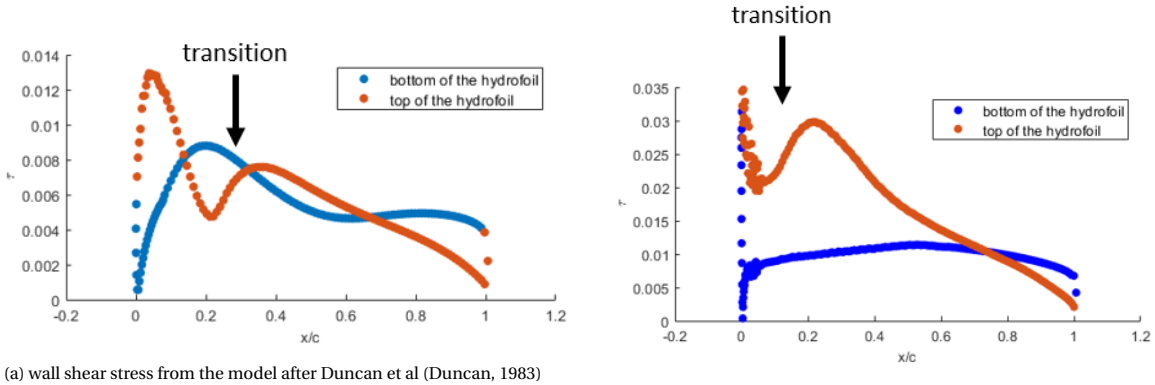

(a) wall shear stress from the model after Duncan et al (Duncan, 1983)

(b) wall shear stress from the model with a large channel depth

Figure 4.18: Wall shear stress at the airfoil. Blue dots represent the top of the hydrofoil. Red is the wall shear at the bottom of the hydrofoil

At the top of the hydrofoil the plots of the wall shear stress show that transition towards a turbulent boundary layer is delayed if a floor is positioned close to the hydrofoil. For case2 (floor at 10c below hydrofoil) the boundary layer starts to transition from laminar to turbulent regime almost immediately. For case1 (floor at 0.86c below hydrofoil) shows that transition starts at approximately 0.2 $\frac{x}{c}$. At the bottom of the hydrofoil, the difference is once again significant. The boundary layer for case2 (floor at 10c below hydrofoil) is laminar along the length of the hydrofoil. The floor in case1 (floor at 0.86c below hydrofoil) induces transition of the

boundary layer at approximately 0.5 $\frac{x}{c}$.
We can conclude that the presence of a floor at 86c below the hydrofoil delays the transitions of the boundary layer on top op of the hydrofoil. Looking back at the wave profiles plotted in figure 4.16, we see that a decrease of the wave amplitude and an slight increase in he wavelength is also induced by positioning a floor at 0.86c below the hydrofoil.
The Reynolds number of the flow is closely related to the location of transition of the boundary layer. To further investigate the relation between the wave profile and the Reynolds number the next paragraph provides the reader with a study on Reynolds number dependence.

Reynolds effect So far we found that the location of transition of the boundary layer from laminar to turbulent regime has an effect on amplitude and wavelength of the wave train. The amplitude increases if transition happens earlier at the hydrofoil. In this paragraph the viscosity of the fluid is changed in order to identify what happens to the free surface for different Reynolds numbers.

Figure 4.22 depicts the free surface profile for three different Reynolds numbers for case2 (floor at 10c below hydrofoil). The Reynolds number is varied by changing the viscosity. This ensures that the Froude number is kept constant. The free surface profile for $Re = 2 \cdot 10^5$ and $Re = 2 \cdot 10^6$ are almost indistinguishable. This indicates Reynolds independence. For $Re = 2 \cdot 10^5$ transition of the boundary layer is still present. We can conclude that transition of the boundary layer is not a dominating factor for Reynolds dependence in the free surface-profile.

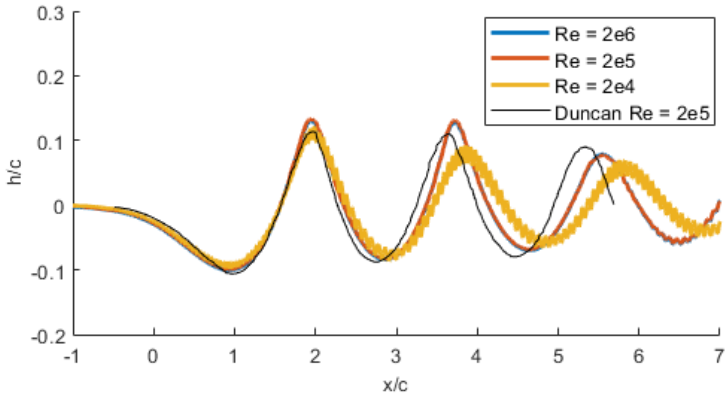

Figure 4.19: First three waves of the wave profile generated by the submerged hydrofoil with submergence $\frac{h}{c} = 0.955$. Black: results from Duncan et al. (Duncan, 1983), yellow: present study $Re = 2 \cdot 10^4$, orange: present study $Re = 2 \cdot 10^5$, orange: present study $Re = 2 \cdot 10^6$. Note that the floor was positioned at 10c below the hydrofoil for these calculations.

Amplitude and wavelength In the previous sections it is shown that modeling of the non-breaking wave train from Duncan et al. (Duncan, 1983) gives different results within literature. Differences are found in amplitude, wavelength and zero point crossings. It is desirable to know which quantities dominate these wave parameters.

In this thesis an inlet value of 0.1 is used for ω. Since the experiment form Duncan et al. (Duncan, 1983) was performed by dragging a hydrofoil trough a stationary fluid, the model should have a very laminar inflow. A laminar flow in RANS models corresponds to a low value for ν_t. The formula for ν_t is given below.

$$\nu_t = \frac{k}{\omega} \tag{4.3}$$

To get a laminar inflow profile we want ν_t to be at least an order of magnitude smaller than ν_w ($\nu_w = 1 \cdot 10^{-6}$). Recall that $k = 0.0015$ in the present model. This gives us a minimum value of $\omega = 1000$. To identify if this difference in ω has had an major impact on the results in previous sections a test is performed in which the wave profile corresponding to $\omega = 0.1, 10$ and 100 are compared. The result is shown in figure 4.20.

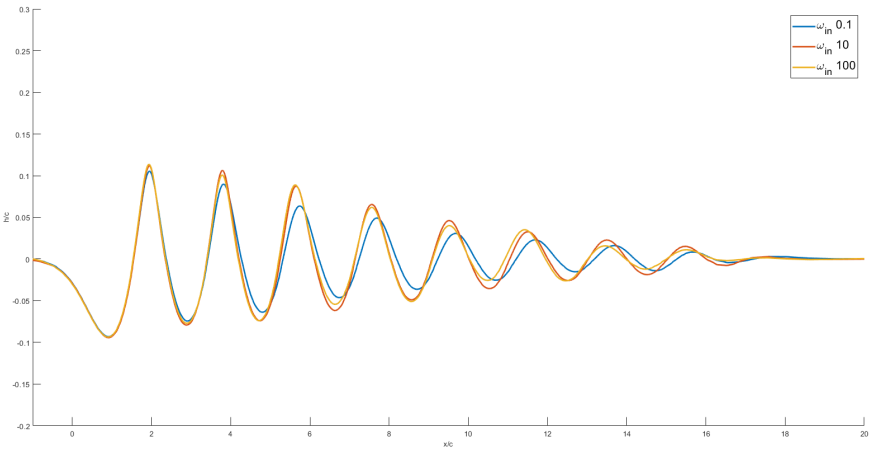

Figure 4.20: Wave profile generated by the submerged hydrofoil with submergence $\frac{h}{c} = 0.955$. Blue: $\omega_{in} = 0.1$, red: $\omega_{in} = 10$ and yellow: $\omega_{in} = 100$

From figure 4.20 a slight increase in wavelength as a function of ω is visible if ω is reduced from 10 to 0.1 . A more notable difference is the attenuation of waves. Attenuation is stronger if the inflow value of the specific rate of dissipation (ω_{in}) is decreased. Between $\omega = 10$ and $\omega = 100$ the difference in wave profile is negligible. For the present thesis this indicates that especially the wave height of the third wave and those that follow are under predicted. The decrease in waveheigth between the second and the third wave crest is approximately 25% for $\omega = 0.1$, while for $\omega = 10$ and $\omega = 100$ this is only 10% The first two waves are expected to be relatively accurately modeled even though ω was chosen relatively low.

The other turbulence parameter in two-equation models is k. De Blasi (De Blasi und Romano, 2000) attributed the difference between their experimental result and that from Duncan et al. (Duncan, 1983) to the inflow turbulence. In RANS simulations k describes the turbulence kinetic energy. This quantity is a function of the turbulence intensity and the inflow velocity as given below. I is a value between which indicates the turbulence level ($\frac{u'}{u}$) of the flow, for laminar flow the value is between 0 and 0.02. This value was used in the present model. To identify whether the inflow turbulence effects the resulting wave train a simulation was carried out for $I = 0.2$ which is considered a very turbulent flow. $I = 0.2$ results in $k \approx 0.15$

$$k = 1.5 I^2 U^2 \tag{4.4}$$

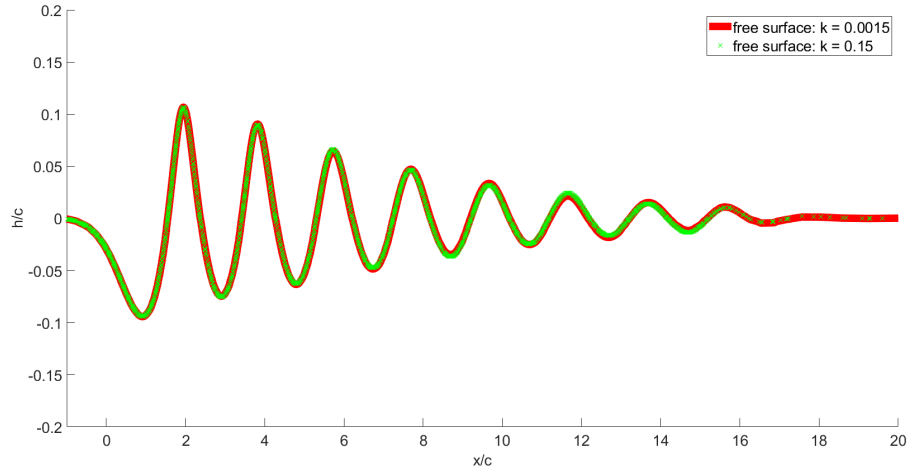

Figure 4.21: Wave profile generated by the submerged naca0012 hydrofoil with submergence $\frac{h}{c} = 0.951$. Blue: $k_{in} = 0.15$, red: $k_{in} = 0.0015$

From figure 4.21 we see that the difference in turbulence kinetic energy has no effect on the wave profile. This suggests that the different result between De Blasi (De Blasi und Romano, 2000) and Duncan (Duncan, 1983) is not caused by the inflow turbulence. the difference in the channel dept is probably reason for the different results.

As discussed in section 4.4.2 Chen et al. (Chen, 2012) argued that viscosity influences the amplitude more than the wavelength. A more viscous flow results in an increase in the wave height. From the Reynolds dependence study in the previous section we can conclude that if the claim made by Chen et al. (Chen, 2012) holds, it only holds for $Re \leq 2 \cdot 10^5$. To quantify this statement a simulation is performed for $Re = 1 \cdot 10^5$ and $2 \cdot 10^5$, and is discussed below.

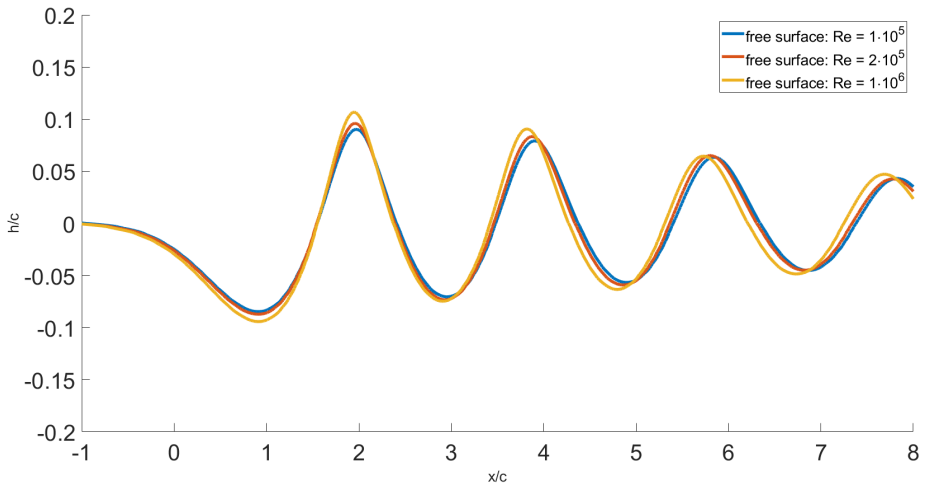

Figure 4.22: Wave profile generated by the submerged hydrofoil with submergence $\frac{h}{c} = 0.955$. Blue: $Re = 1 \cdot 10^5$, red: $Re = 2 \cdot 10^5$ and yellow: $Re = 2 \cdot 10^6$

Figure 4.22 tells us that the amplitude is effected more than the wavelength if the Reynolds number is changed. Higher Reynolds numbers result in shorter wavelengths and an increase in the wave height. If the Reynolds number is increased form $Re = 1 \cdot 10^5$ to $2 \cdot 10^5$ the amplitude increase by approximately 6% while the wavelength reduces by less than 0.5%. The attenuation of waves is stronger for higher Reynolds numbers. The attenuation for $Re = 1 \cdot 10^6$ was approximately 10% stronger than for $Re = 2 \cdot 10^5$.

Submergence depth Duncan and his colleagues (Duncan, 1983) use the Froude number based on the chord length (Fr_c). Duncan notes that the Froude number based on the submergence depth (Fr_h) might be more relevant. In the present study a non-breaking simulation has been performed for two submergence depths: $\frac{h}{c} = 1.034$ and $\frac{h}{c} = 0.955$. In terms of Froude number this is: $Fr_h = 0.58$ and $Fr_h = 0.56$. Figure 4.23 depicts the wave profile from these two cases.

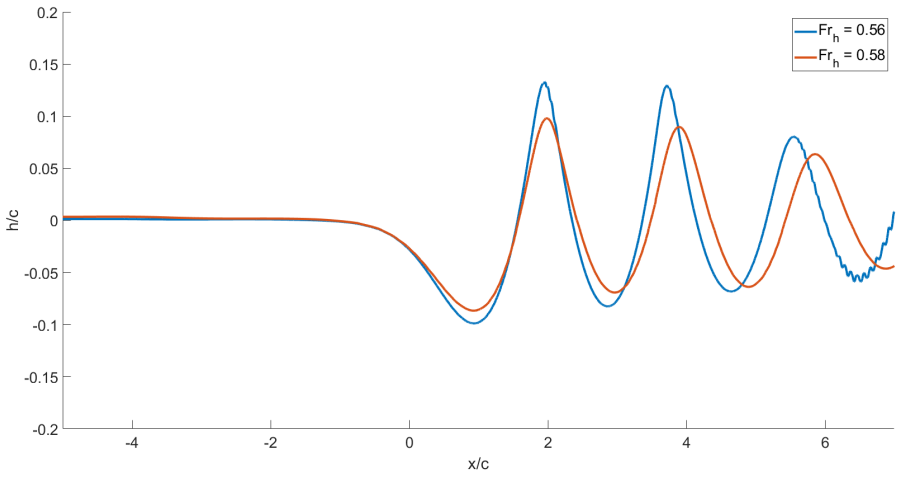

Figure 4.23: Wave profile generated by the submerged naca0012 hydrofoil with submergence for blue: $Fr_h = 0.56$ and red: $Fr_h = 0.58$. both at $Re = 1 \cdot 10^6$

From figure 4.23 we see that the amplitude and of the wave train decreases and the wavelength increases if Fr_h is increased. The decrease in the first hollow is less significant with 12.5% than the increase in the first crest which is 26% lower. The wavelength is approximately 7% longer if Fr_h is increased by 0.02.

Conclusion In conclusion we now know that the effect of the inflow value of k is negligible on the resulting wave train. The inflow value of ω mainly effects the attenuation of the wave train in stream wise direction. smaller values for ω at the inlet result in stronger attenuation. For $\omega \geq 10$ the attenuation of waves is no longer influenced by increasing the inflow value of ω. Changing the Reynolds number of the flow has an effect on both the wavelength and the wave amplitude. Here an increase in the Reynolds number results in an larger amplitude and an increase in wavelength. The effect of changing the Reynolds number of the flow has a greater impact on the amplitude than on the wavelength. If the Froude number based on submergence depth is altered the wave train effected much more than the previously discussed parameters. Both the amplitude and the wavelength increase if Fr_h is reduced. Table **??**ummarizes the quantitative effect of changing

comparison Chen et al. The results from Chen et al. (Chen, 2012), raise some questions. Chen and Chwang (Chen, 2012) tried to model the free surface for a submergence of $\frac{h}{c} = 1.034$ with $Re = 0.5 \cdot 10^4, 2.0 \cdot 10^4$ and $3.0 \cdot 10^4$. For $Re = 3.0 \cdot 10^4$ The free-surface profile from Chen and Chwang at $Re = 3.0 \cdot 10^4$ is surprisingly similar to the experimental result from Duncan et al. (Duncan, 1983) where the submergence was $\frac{h}{c} = 1.034$ and $Re = 2 \cdot 10^5$.
The Reynolds number used by Chen et al. results in purely laminar flow. they used a relatively small domain, 6.5 chord lengths in front of the hydrofoil and 10 chord lengths behind the foil. In their study a damping

region was applied at both sides of the domain. Both regions span approximately 2 chord lengths in the flow direction. Chen et al. (Chen, 2012) found an instationary wave profile. Their results are time averaged between $t = 15$ and $t = 26$. The model used in this thesis doe snot show an instationary wave profile. The results from the present study are therefore not time averaged.
Figure 4.24 visualizes the free surface waves from the present study together with the result from Chen and Chwang (Chen, 2012). The current model was solved for Chen's Re number with a laminar and a turbulence model. This was done because the difference between the laminar model and the result from Chen and Chwang raised the question if they accidentally used a turbulence model in their study.
from figure 4.24 it is clear that the turbulence model did not significantly effect the wave profile. The wavelength of the present study is of the same order as the result from Chen et al. (Chen, 2012). The amplitude and horizontal location of minima and maxima are different.

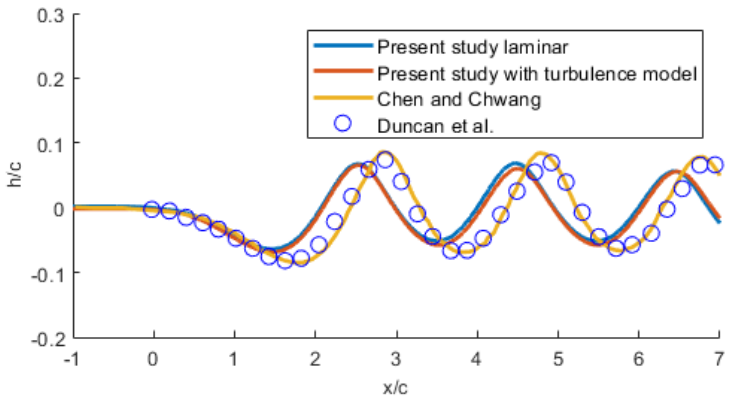

Figure 4.24: free surface from, Chen in yellow, present study laminar in blue and the present study with turbulence model in red. All with $Re = 3 \cdot 10^4, h = 1.034$. the Blue circles represent the result form Duncan et al. $\frac{h}{c} = 1.034$ and $Re = 2 \cdot 10^5$. In the present study the same geometry as that from the experiment by Duncan is used, this geometry is given in figure 4.15a

In their study, Chen and Chwang plot velocity and pressure over a vertical line beneath the first wave crest at $t = 26$. Both the laminar case and the one with turbulence model are compared against the results from Chen and Chwang (Chen, 2012). This is done to show if Chen and Chwang accidentally used a turbulence model. The comparison between the laminar run in the present study and the results from Chen and Chwang are plotted in Figures 4.25 a, b and c.

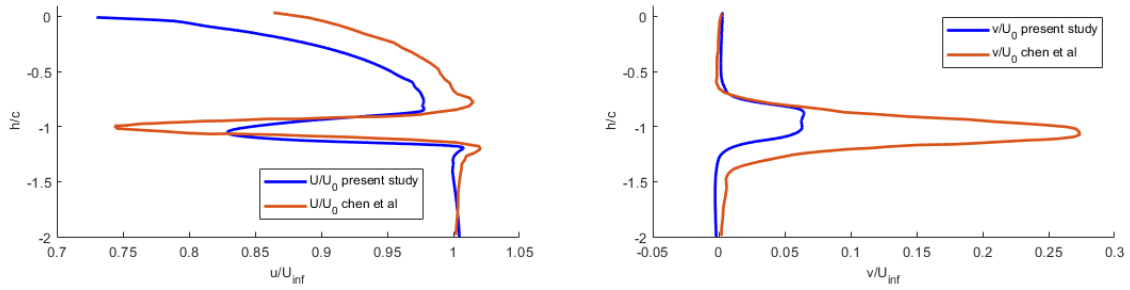

(a) Horizontal velocity normalized by the inflow velocity

(b) Vertical velocity normalized by the inflow velocity

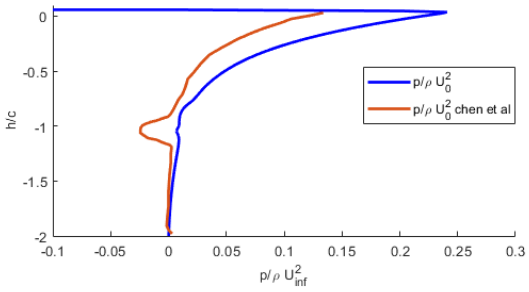

(c) Pressure normalized by density and inflow velocity

Figure 4.25: comparison of field variables plotted over a vertical line underneath the first wave crest. comparison between, blue:the present study on the grid also used for the comparison with Duncan's experiments, without turbulence model and red: Chen and Chwang (Chen, 2012) with $Re = 3 \cdot 10^4$ at $t = 26s$

From figure 4.25a we see that the magnitude of the velocity for our results is underestimated between the free surface and the top of the wake behind the hydrofoil. This is probably because the interaction between fluids at the free surface has effected the velocity in the present study. Chen and Whang did not solve the the air phase in their study. This does not explain why the velocity inside the wake is higher in the present study compared to Chen et al. Differences in the wake are also clear for the vertical velocity component and the pressure.

Figure 4.26 Depicts the same vertical line plot for the same parameters as discussed above, but this time for the case in which a turbulence model ($k-\omega SST$) was used. It is clear that all parameters show a closer resemblance to the result form Chen and Chwang (Chen, 2012). It is therefore expected that Chen et al. (Chen, 2012) incorrectly used a turbulence model.

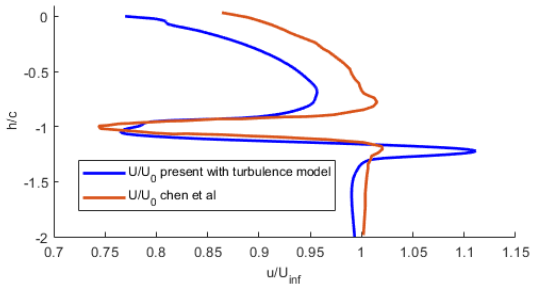

(a) Horizontal velocity normalized by the inflow velocity

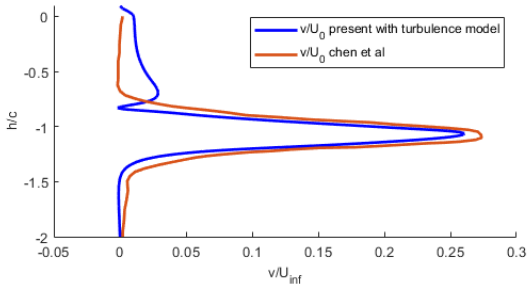

(b) Vertical velocity normalized by the inflow velocity

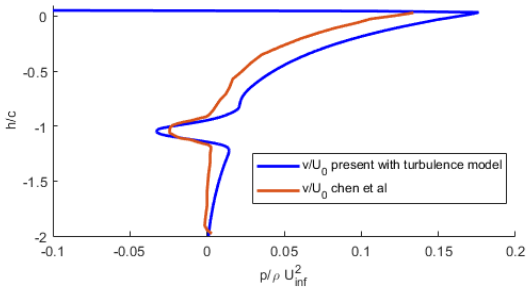

(c) Pressure normalized by density and inflow velocity

Figure 4.26: comparison of field variables plotted over a vertical line underneath the first wave crest. comparison between, blue:the present study using the same geometry as used for comparing the results from Duncan.with turbulence model and red: Chen and Wang (Chen, 2012) with $Re = 3 \cdot 10^4$ at $t = 26s$

Even though the flow parameters below the first wave crest in figures 4.26 a, b and c show resemblance, the wave profile in figure 4.24 is completely different. Chen and his colleagues found an instationary wave profile. This was not found in the present study. A possible explanation for the instationary wave profile from Chen et al. (Chen, 2012) is the small domain and sponge layer size. If the generated waves are not completely damped they can reflect at the outlet boundary. This refection can effect the resulting wave dynamics. As discussed in the previous paragraph, a small domain size is expected to result in an overall greater amplitude for the wave profile.

4.4.3. multiphase breaking

Duncan analyzed breaking waves in his article (Duncan, 1983). Figure 4.27 gives a schematic representation of the breaking wave.

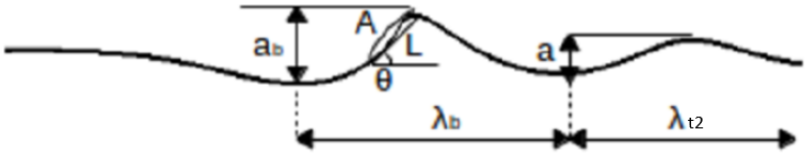

Figure 4.27: geometrical parameterization of a breaking wave with trailing waves from (Duncan, 1983) a_b is the amplitude of the breaking wave, A denotes the area of the breaker, θ is the angle of the breaking wave, a is the amplitude of the first trailing wave, λ is wavelength of the breaking wave, λ_{2t} is the wavelength of the first trailing wave.

Breaking waves occur for low submergence of the hydrofoil. Duncan found that transition from non-breaking to breaking waves happens over a change of submergence of 0.025 chord lengths. Duncan does not mention the exact range. He does present two plots of the free surface in the transition region, at submergence $\frac{h}{c} = 0.955$. In this transition region a steady breaking wave can be triggered by artificially creating a surface current. Duncan did this by dragging a cloth over the water surface. The resulting breaking wave is a spilling breaker. Figure 4.28 depicts the four typical ways a wave can break.

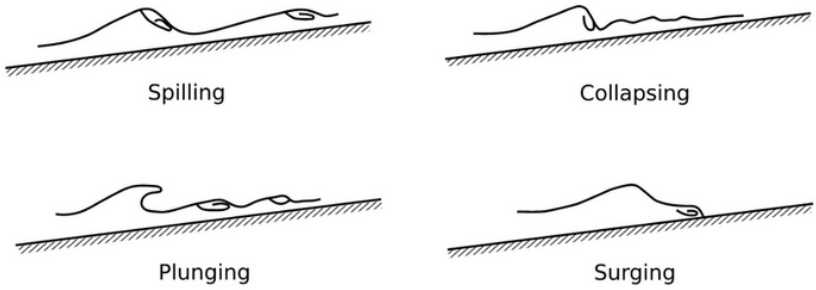

Figure 4.28: Different types of waves breaking. Picture taken from (Fleit, 2015)

According to Duncan, the stability criterion of the free surface wave is the slope. Breaking occurs for steep waves where the transition (unstable) region corresponds to $\theta = 17°$. Duncan reported that breaking waves show a typical back and forward motion with a frequency defined by the wavelength. Duncan derived two expressions for the wavelength and frequency, they are given below.

$$U_0 = 4.4\sqrt{\frac{g\lambda_b}{2\pi}} \tag{4.5}$$

$$T_b = 4.4\frac{\lambda}{U_0} \tag{4.6}$$

Lupieri(Lupieri und Contento, 2015) tried to model the experiment from Duncan. He states that due to the oscillating movement of the breaking wave, the results need to be time averaged. The averaging procedure is done as follows: Free surface elevation at any longitudinal position is averaged over a time window. The average is taken of the smallest and the greatest elevation on each longitudinal position. The time window is specified by formula 4.4.3.
In this study an effort is made to model the spilling breaker from Duncan et al. Table 4.19 list the main geometrical parameters used in this case.
Figure 4.30 is a plot of the result from Duncan(red)(Duncan, 1983) and the time averaged result from the present study. Lupieri (Lupieri und Contento, 2015) remarks that Duncan measured within the foam region. The actual location of measurement is not known or described by either Duncan or Lupieri. In the present model this is accounted for by plotting for $\alpha = 0.5$ in blue, the outer regions $\alpha = 0.99$ and $\alpha = 0.01$ are given in black. Figure 4.30 shows the result as discussed above, compared against the result from Duncan et al. (Duncan, 1983) and those from Lupieri et al. (Lupieri und Contento, 2015).

Table 4.19: Geometrical parameters of the spilling breaker cases evaluated in this thesis.

case	$\frac{x}{c}$ range	$\frac{y}{c}$ range	$\frac{h}{c}$	α
case3	-20 40	-1.769 20	0.911	5°

As described in chapter 2: Related work 2, Duncan analyzed a spilling breaker. Figure 4.29 once again shows the spilling breaker we want to model.

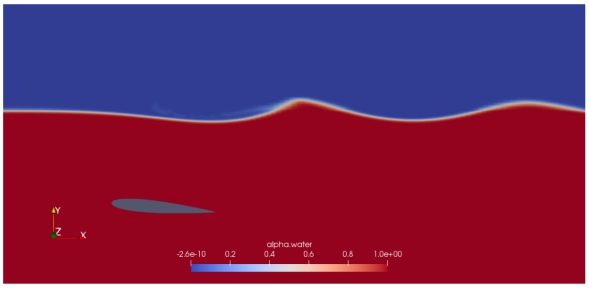

Figure 4.29: example of a spilling breaker and resulting wave train, generated by a submerged naca0012 hydrofoil. picture from: (Prasad u. a., 2015)

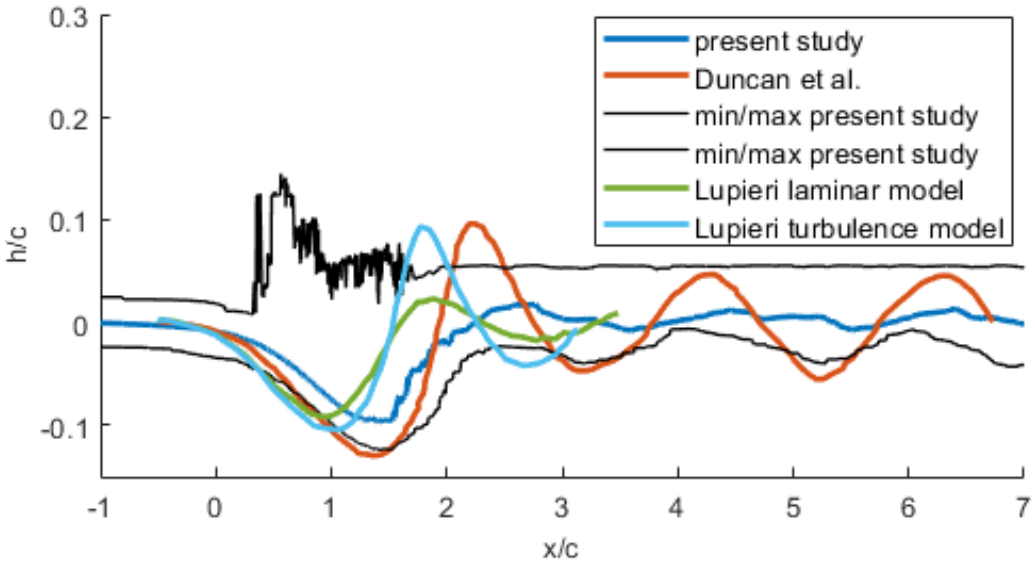

Figure 4.30: free surface elevation compared to the result from Duncan et al. (Duncan, 1983). $Fr = 0.567$, $\frac{h}{c} = 0.991$

The model shows a different kind of breaking than the one found by Duncan. This was also reported by Lupieri. The result from Lupeiri et al. (Lupieri und Contento, 2015) looks much more like those from Duncan.

It is import to note that the result form lupieri are for a different submergence depth $\frac{h}{c} = 0.783$. These large differences in wave profiles for breaking waves, show that RANS simulations are not suited for modeling breaking waves. Lupieri refers to the over estimation of the eddy viscosity in 2-D RANS models. This results in incorrect predictions of the wave profile.

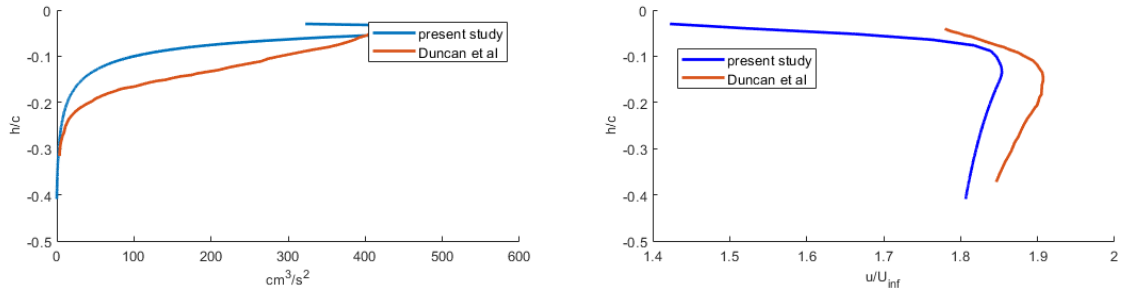

(a) total head defect beneath the second hollow after the breaker, compared to the result from Duncan et al. (Duncan, 1983). $Fr = 0.567$, $\frac{h}{c} = 0.991$

(b) Horizontal velocity beneath the second hollow after the breaker, compared to the result from Duncan et al. (Duncan, 1983). $Fr = 0.567$, $\frac{h}{c} = 0.991$

Figure 4.31: Normalized horizontal velocity and pressure compared against Duncan

The total head defect h_t and normalized horizontal velocity profile is plotted in figure 4.31b and 4.31a respectively. Equation 4.7 is the formulation of the total head defect. Here $p_{rgh2}(y)$ is the reduced pressure at any location y beneath the second trough. $p_{rgh1}(y)$ is the reduced pressure in the undisturbed flow upstream of the hydrofoil.

$$h_t(y) = p_{rgh2}(y) - p_{rgh1}(y) \tag{4.7}$$

Both show that the current model underestimates these values compared to the result from Duncan. This is probably due to the different type of breaking. In the current model breaking is more violent, resulting in more momentum loss. As a result of lost momentum the horizontal velocity profile is slowed down. The reduced wave elevation results in less head defect, this is clearly shown in figure 4.31a. To investigate if this remarkable difference in breaking is caused by flow detachment from the hydrofoil, the wall shear stress is plotted. Detachment from the hydrofoil is visualized by a negative value for the wall shear stress. Wall shear stress form the present model is plotted in Figure 4.32. The lack of negative values for the wall shear stress proves that the flow is attached in the breaking case.

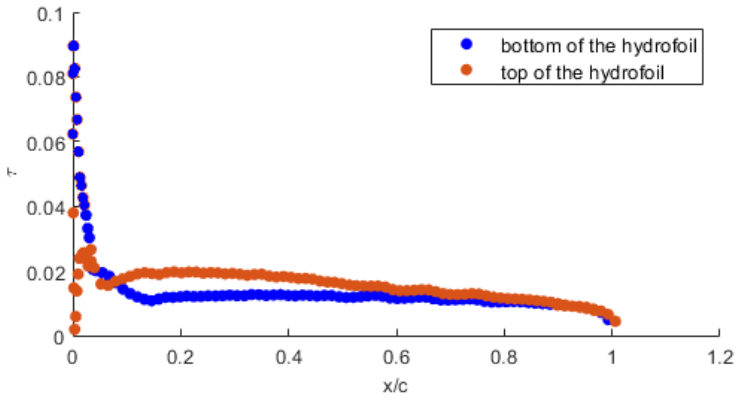

Figure 4.32: τ at the airfoil, $Fr = 0.567$, $\frac{h}{c} = 0.991$,$Re = 1.8 \cdot 10^5$

From the breaking case we can conclude that modeling of breaking waves using RANS VOF is difficult. To find the spilling breaker for the present model, the Froude number has been reduced to 0.5 and incrementally increased. The spilling breaker was found for $Fr = 0.53$ and $Re = 1.8 \cdot 10^5$. The free surface profile from this result is again compared against the result from Duncan et al. (Duncan, 1983). Figure 4.33

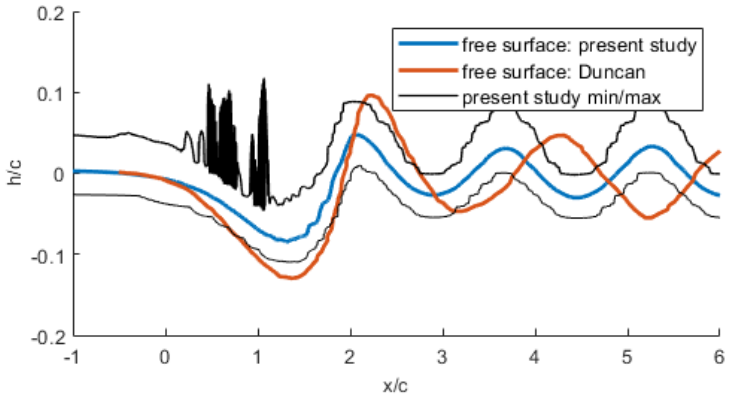

Figure 4.33: free surface profile from present study spilling breaker, $Fr = 0.53$ and $Re = 1.8 \cdot 10^5$ compared against Duncan (Duncan, 1983)

Even if the type of breaking is comparable to that from Duncan et al. (Duncan, 1983), a completely different wave profile is found. This again shows that more research on 2-D RANS models is necessary before we can confidently use them for modeling breaking waves.

5

Conclusions and recommendations

This thesis was conducted in order to find the accuracy of RANS models for simulating free surface waves generated by a shallowly submerged naca0012 hydrofoil at a moderate angle of attack of 5°. OpenFoam is used as programming software, within this software the volume of fluid (VOF) approach is used to model the interface between the two immiscible fluids. For modeling of turbulent flow the two equation model, k-ωSST from Menter et al. (Menter, 1992) is used.

The model setup was tested by conducting fully developed channel simulations and single phase airfoil tests. The accuracy of the model was evaluated using experimental and numerical data available from other researchers, with the main focus on experimental results from Duncan at al. (Duncan, 1983). Different relevant parameters are isolated and evaluated to investigate their effect on the free surface-profile.
This Chapter contains a concluding remark on the research questions that are stated in the first chapter of this thesis. Thereafter a number of recommendations for future work is given.

5.1. Conclusion

The conclusion of this research is formulated using the proposed research question and subquestions.

> How do relevant fluid and geometrical properties effect the wave profile generated by a shallow submerged naca0012 hydrofoil?

To answer this research question a number of subquestions are formulated that serve as a guidance towards answering the research question above.

> What grid dimensions and domain sizes are necessary for accurate representation of the flow? This is discussed in section: Domain size, grid and sponge layer
>
> How does the wave profile respond to different Reynolds numbers? This is discussed in section: Reynolds dependency
>
> To what degree does turbulence in the mean flow effect the final wave train? This is discussed in section: Mean flow turbulence)
>
> What effect does the submergence of the hydrofoil have on the wave dynamics? This is discussed in section: Submergence
>
> How accurate is the representation of breaking waves using RANS models? This is discussed in section: Breaking waves

Before the discussion on the research questions is given, we first discuss the reference data that is used. The way the numerical model is tested is also described before discussing the research questions.

5.1.1. Discussion of the reference data

This thesis focused on modeling the results from Duncan et al. (Duncan, 1983). During this work we found that the paper presented by Duncan et al. does contain a number of uncertainties. These will be summarized in this section.

The first thing that misses in the description of the experimental setup from Duncan, is the horizontal positioning of the hydrofoil in an axis system. It is expected that Duncan took the hydrofoil center as the horizontal 0 point. Duncan does give a number of measurement errors, but there lacks a set of error bars in their results. De Blasi (De Blasi und Romano, 2000) also performed experiments on a shallowly submerged naca0012 hydrofoil. De Blasi did present error bars in their results. The experiments from Duncan et al. are performed at $Re = 2 \cdot 10^5$. For external flows at $Re \approx 2 \cdot 10^5$ we expect transition of the boundary layer regime from laminar to turbulent. There is no discussion on the presence of transition by Duncan. The present study has shown that transition of the boundary layer is present. We also found that transition is not the dominating parameter for Reynolds dependence. Reynolds dependency is further discussed in section 5.1.4: Reynolds dependency.
The experimental setup from Duncan has the basin floor fixed at 0.86c below the hydrofoil. Duncan mentioned the effect on the local flow at the hydrofoil. Duncan does assume that position of the floor in their experiments does not effect the wave dynamics. This assumption has lead other researchers to position the basin floor far from the hydrofoil. We found that the position of the floor with respect to the hydrofoil does significantly change the resulting free-surface profile.
An estimation of the wave making drag is given by Duncan et al. But their assumption that the other types of drag are negligible is shown to be false. Lupieri et al. (Lupieri und Contento, 2015) noted that the results on breaking waves presented by Duncan et al. are time averaged solutions. Duncan does not mentioned that their breaking wave results are time averaged.

5.1.2. Testing the numerical model

The k-ωSST turbulence model that is used in this thesis was tested using the fully developed channel measurements from Moser et al.(Moser u. a., 1999). We formulated the Reynolds number based on the boundary layer thickness $Re_\delta = \frac{U \cdot \delta}{\nu}$. With Re_δ we could use the channel flow results to predict the accuracy of the k-ωSST for the hydrofoil flow. We found that for $y^+ = 0.7$ the velocity profile is very accurately represented. Within the buffer layer $y^+ = 15$ we found that both a wall function and a fixed value prescribed at the wall resulted in a wrongly predicted velocity profile. For $y^+ = 60$ a strong overestimation of the velocity profile was found. This is probably due to the relatively low Reynolds number. The log layer was smaller than $y^+ = 60$ resulting in an under prediction of the wall shear. In the hydrofoil tests a fixed value of 0 at the wall is used for k at the wall with an y^+ of 0.07.

To verify the interFoam solver from openFoam we conducted several tests with an airfoil in a single fluid. We simulated the exact same flow on the same grid for both the interFoam and simpleFoam solver. A comparison was made between the pressure coefficient from interFoam, simpleFoam and JavaFoil. We observed an underestimation of the pressure coefficient near the stagnation point for both the SimpleFoam and the InterFoam results. Near the tail of the hydrofoil the InterFoam solver gave a better fit to the Javafoil result comapred to the SimpleFoam solver. The InterFoam solver showed an unsteady flow profile, where flow separation and reattachment was visible. The InterFoam solver probably overestimates the adverse pressure gradient resulting is these separation bubbles at the surface of the airfoil. Another single phase test was performed using the grid that was eventually used in the multiphase test cases. The comparison between the pressure coefficient from this grid and the javaFoil result did not show an unsteady flow profile. It is therefore expected that the separation bubbles will not be present in the multiphase case. The previously mentioned expectation of presence of separation of the boundary layer was tested on the single phase airfoil. By plotting the wall shear stress we found that transition was indeed present for $Re = 2 \cdot 5^(10)$.

5.1.3. Domain size and grid and sponge layer

What grid dimensions and domain sizes are necessary for accurate representation of the flow?

We found that the free surface in VOF models is very sensitive to the aspect ratio between neighboring cells. If the aspect ratio is to large, "wiggles" in the form of a very small wavelength wave train will show at the interface. If the aspect ratio is kept below 1.05 the free surface does not show nonphysical short wavelength

waves.
From section: Effect of grid and domain size and the comparison with Chen et al. (Chen, 2012) we observed a correlation between a short domain size and an increase in free surface wave amplitude. The attenuation of the wave train is said to be stronger if the cells have a to large increase in cell size toward the outlet. (Walker u. a., 2004). This was also found int he present study.
We evaluated the importance of a correctly defined domain and grid distribution. We concluded that damping of waves must be enforce by other numerical options. From other articles we found that a sponge layer was very important if a reasonable free surface profile has to be modeled. In the present study we found that the strength of the sponge layer is limited. If the damping force of the sponge layer is to strong, waves can reflect from the sponge layer. A damping force of $\lambda = 0.1$ over a length of 10 chord length in stream wise direction and $\lambda = 0.1$ over a length of 5 chord length in upstream direction is used. The combination of increase in grid size and the sponge layer resulting in complete damping of waves towards both the inlet and the outlet.

5.1.4. Reynolds dependency

How does the wave profile respond to different Reynolds numbers?

In the present thesis Reynolds independence was found between $Re = 2 \cdot 10^5$ and $2 \cdot 10^6$. This Reynolds dependency was performed on a model where the basin floor was modeled at 10c below the hydrofoil. The question raised if transition of the boundary layer regime from laminar to turbulent is the dominating flow characteristic for Reynolds independence. Transition of the boundary layer is still present for $Re = 2 \cdot 10^5$ at approximately 0.2c at the top of the hydrofoil. For $Re = 2 \cdot 10^6$ the boundary layer is completely turbulent. Reynolds dependency within this regime is thus not dominated by the transition of the boundary layer. For the other case, which was modeled after the experimental setup from Duncan et al. with the basin floor at 0,86c below the hydrofoil. (Duncan, 1983) the effect of the Reynolds number below Reynolds independence was tested. From this test we found that a reduction of the Reynolds number results in a decrease in the wave elevation and a slight increase in the wavelength. The amplitude of the first wave is 6% smaller if the Reynolds number is reduced from $Re = 2 \cdot 10^5$ to $Re = 1 \cdot 10^5$ while the wavelength increases by less than 0.5% Attenuation of the wave train was found to be stronger for higher Reynolds flows. The attenuation for $Re = 1 \cdot 10^6$ was 10% stronger than for $Re = 2 \cdot 10^5$.

5.1.5. Mean flow turbulence

To what degree does turbulence in the mean flow effect the final wave train?

The experiment performed by Duncan et al. was performed by dragging a hydrofoil through a stationary water basin. De Blasi and Contento (De Blasi und Romano, 2000) argued that the difference between their result and that from Duncan was the result of a free surface boundary layer. This boundary layer resulted from their experiments that where performed in a circulating water channel.
The mean flow in a circulating water channel will never be laminar like the stationary basin from Duncan. The question raised to what degree the mean flow turbulence parameters changes the resulting free-surface profile. In the k$-\omega$SST model that was used turbulence properties are described by k and ω. Both have been changed to see what effect these changes had on the free-surface.

k In the initial model we used $k = 0.0015$ which corresponded to a turbulence intensity of $\approx 2\%$. We later ran a model for $k = 0.15$ corresponding to a turbulence intensity of $\approx 20\%$. From the free surface profile we observed that this difference in inflow did not change the free-surface profile at all. Therefore the assumption that turbulence due to their circulating water channel from de Blasi et al. is proven to be wrong.

ω To identify the effect of ω on the free-surface profile we tested several inflow values for ω. It was shown that attenuation of waves was stronger if ω is reduced from 10 to 0.1. The attenuation was strongest between the second and 3 wave. the reduction of the amplitude between the second en third wave for $\omega = 10$ was only about 10% while for $\omega = 0.1$ this drop was $\approx 25\%$. Between $\omega = 10$ and $\omega = 100$ the difference in wave profile was small.

5.1.6. Submergence

What effect does the submergence of the hydrofoil have on the wave dynamics?

Duncan explained that they used the Froude number based on the chord length in their study. They also noted that it might have been better to use the Froude number based on the submergence depth (Fr_h) of the hydrofoil. In this thesis a comparison is made between $Fr_h = 0.56$ and 0.58. The effect of changing Fr_h by only 0.02 was significant. Reducing Fr_h results in an increase of the height of the first and second crest of approximately 20%. A smaller increase of 15% of the depth of the first and second trough is also found. Apart form the change in wave elevation the wavelength is approxiamtely 7% shorter if Fr_h is reduced by 0.02. This reduction of the wavelength is in accordance with the breaking criterion proposed by Duncan et al. This is further discussed in the next section.

5.1.7. Breaking waves

How accurate is the representation of breaking waves using RANS models?

In the present study we tried to model the spilling breaking wave from Duncan's results. For the exact same geometrical parameters a much more violent breaking wave was found. The wall shear stress was plotted to see if separation of the boundary layer was present in the breaking case. The boundary layer turned out to stay attached to the hydrofoil. The Froude number Fr_c was lowered incrementally until a spilling breaker like the one described by Duncan et al. was found. A spilling breaker was found at $Fr_c = 0.53$, $Re = 1.8 \cdot 10^5$ with submergence $\frac{h}{c} = 0.991$. While the type of breaking is identical, the wave profile was significantly different from the result from Duncan. It is therefore expected that The current model is not suited for simulating breaking waves. This was also concluded by Lupieri et al. (Lupieri und Contento, 2015)

5.1.8. Model accuracy

Now that we have discussed all parameters that might effect the free-surface profile we can conclude with the best possible representation of the free-surface profile from Duncan's results. Figure 5.1 depicts the result from the present model for $\alpha = 5$,($Re = 2 \cdot 10^5$), $\frac{h}{c} = 0.955$, $\frac{D}{c} = 0.86$, with $\omega = 10$ at the inlet. The black line represents the wave profile from Duncan (Duncan, 1983).

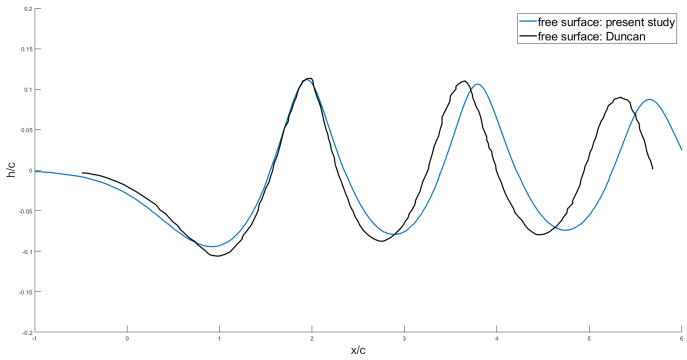

Figure 5.1: first three waves of the wave-profile generated by the submerged hydrofoil. The blue line is the present result: $\alpha = 5$,($Re = 2 \cdot 10^5$), $\frac{h}{c} = 0.955$, $\frac{D}{c} = 0.86$, with $\omega = 10$ at the inlet. The black Line is the wave profile from Duncan et al. (Duncan, 1983)

From figure 5.1 we see that the first hallow is underestimated by approximately 13% the first crest is almost identical to the result from Duncan. The second and third hollow are both underestimated by approximately 10%. The second and third crest slightly deviate in amplitude from the result by Duncan. Both are under predicted by about 4% Apart from the amplitude, there is also a difference in the wavelength between the numerical result form this study and the experimental result from Duncan. In the present study the wavelength is over estimated by approximately 10%.

5.2. Future work

RANS models are widely used in industry, they provide reasonable estimation of flows for many engineering subjects. This thesis supplies the users of these models with valuable knowledge on the uncertainty of wave profiles modeled within RANS models. More knowledge on the manipulation of the free-surface waves is gained from this study. This is done by isolating important dimensionless quantities and showing how changing these dimensionless parameters effects the free-surface wave profile.

All quantities that were evaluated in this research effected the amplitude of the free surface-waves more than the wavelength . One length scale that has not been altered in this thesis is the chord length. We want a complete picture of the effect of all length scales, therefore the effect of the Froude number based on the chord length Fr_c must also be evaluated.

The transition of the boundary layer has been shown to change for different situations in the present study. An investigation of the effect of the transition location on the free-surface waves could give valuable insight in the effect of boundary layer transition on free-surface flows. By artificially creating a transition point the effect of transition can be isolated from other fluid dynamic properties. From the single-phase test we found a significant difference in the pressure coefficient from the SimpleFoam solver versus the InterFoam solver. The reason for the difference is still unknown and it is recommended to investigate where this difference comes from.

For the maritime industry there is a strong motivation to find ways of manipulating the free-surface profile generated by submerged bodies. An interesting way of manipulating the free-surface profile generated by 2D hydrofoils is suction and blowing. Here the surface of the hydrofoil contains small gaps trough which a fluid can by sucked inward of expelled outwards. Suction and blowing can change the lift of the hydrofoil hereby possibly also changing the free-surface waves.

Appendix

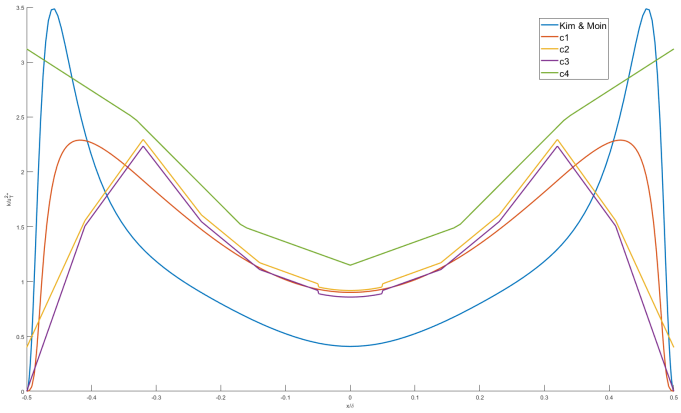

Figure 5.2: comparison of k between DNS performed by Kim and Moin (Kim u. a., 1987) , and present study for $Re = 330$ blue: data from Moser etal. (Moser u. a., 1999) , red: c1, purple: c2, yellow: c3 green: c4. The green line at the bottom represents the simulation with $y^+ = 60$. This run did not converge because there where only 2 cells orthogonal to the flow direction. Corresponding y^+ values: c1:0.7, c2:15 ,c3:15 ,c4:60.

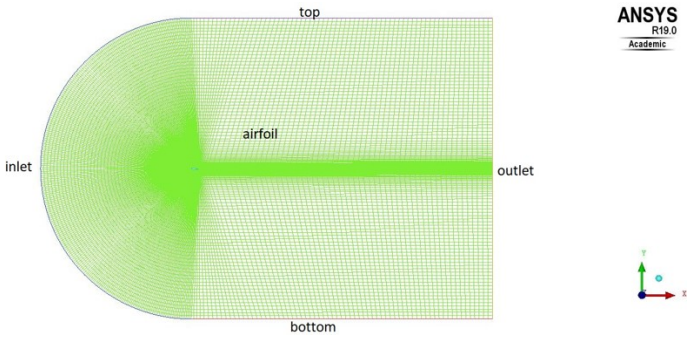

Figure 5.3: The mesh used for the single phase test case

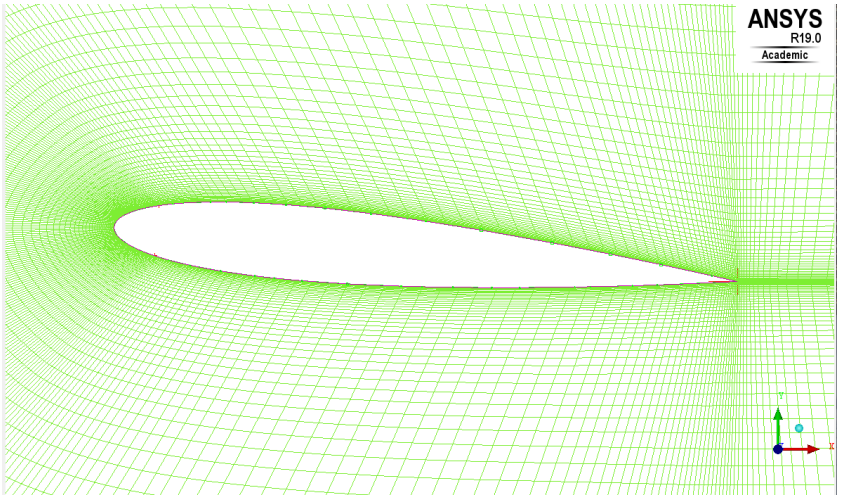

Figure 5.4: Drag from the simpleFoam case

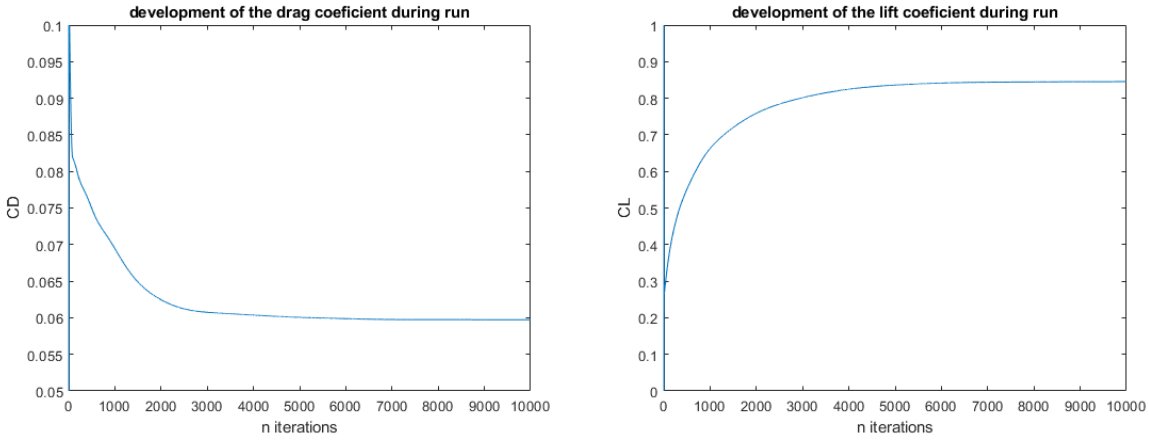

(a) example of drag convergence from the simpleFoam case

(b) Example of lift convergence from the simpleFoam case

Figure 5.5: Lift and drag from simpleFoam model (Prasad u. a., 2015)

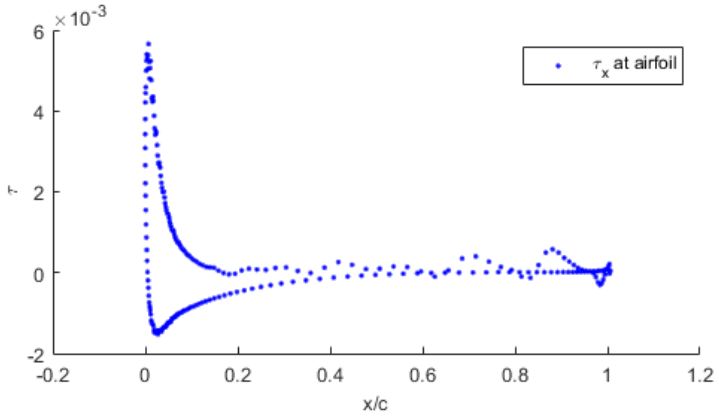

Figure 5.6: Plot of the wallshear stress from the interfoam run on the c-type grid

Bibliography

[Bernard 1986] BERNARD, Peter S.: Limitations of the near-wall k-epsilon turbulence model. In: *AIAA journal* 24 (1986), Nr. 4, S. 619–622

[Chen 2012] CHEN, Zhi-Min: A vortex based panel method for potential flow simulation around a hydrofoil. In: *Journal of Fluids and Structures* 28 (2012), S. 378–391

[De Blasi und Romano 2000] DE BLASI, Paolo ; ROMANO: Experimental study of breaking wave flow field past a submerged hydrofoil by LDV. In: *International Journal of Offshore and Polar Engineering* 10 (2000), Nr. 04

[Deshpande u. a. 2012] DESHPANDE, Suraj S. ; ANUMOLU, Lakshman ; TRUJILLO, Mario F.: Evaluating the performance of the two-phase flow solver interFoam. In: *Computational science & discovery* 5 (2012), Nr. 1, S. 014016

[Di Mascio u. a. 2007] DI MASCIO, A ; BROGLIA, R ; MUSCARI, R: On the application of the single-phase level set method to naval hydrodynamic flows. In: *Computers & fluids* 36 (2007), Nr. 5, S. 868–886

[Duncan 1983] DUNCAN, James H.: The breaking and non-breaking wave resistance of a two-dimensional hydrofoil. In: *Journal of Fluid Mechanics* 126 (1983), S. 507–520

[Eppler 1963] EPPLER, Richard: Praktische Berechnung laminarer und turbulenter Absauge-Grenzschichten. In: *Archive of Applied Mechanics* 32 (1963), Nr. 4, S. 221–245

[Eppler 1978] EPPLER, Richard: Turbulent airfoils for general aviation. In: *Journal of Aircraft* 15 (1978), Nr. 2, S. 93–99

[Eppler und Somers 1980] EPPLER, Richard ; SOMERS, Dan M.: A computer program for the design and analysis of low-speed airfoils. (1980)

[Fleit 2015] FLEIT, Gábor: *Numerical modeling of complex free surface flows*, Dissertation, 06 2015

[Hepperle 2019] HEPPERLE, Martin: *javaFoil*. 2019. – URL `https://www.mh-aerotools.de/airfoils/javafoil.htm`

[Hickel 2018] HICKEL, Prof.dr. S.: *CFD fot aerospace engineers*. 2018

[Hirt und Nichols 1981] HIRT, Cyril W. ; NICHOLS, Billy D.: Volume of fluid (VOF) method for the dynamics of free boundaries. In: *Journal of computational physics* 39 (1981), Nr. 1, S. 201–225

[Kim u. a. 1987] KIM, John ; MOIN, Parviz ; MOSER, Robert: Turbulence statistics in fully developed channel flow at low Reynolds number. In: *Journal of fluid mechanics* 177 (1987), S. 133–166

[Kundu 2013] KUNDU, Pijush K.: *Fluid Mechanics*. Academic Press, 2013. – URL `http://search.ebscohost.com.tudelft.idm.oclc.org/login.aspx?direct=true&db=nlebk&AN=596581&site=ehost-live`. – ISBN 9780124287709

[Kuron 2015] KURON, Mike: *3 Criteria for Assessing CFD Convergence*. 2015. – URL `https://www.engineering.com/DesignSoftware/DesignSoftwareArticles/ArticleID/9296/3-Criteria-for-Assessing-CFD-Convergence.aspx`

[Lalli 1997] LALLI, F: On the accuracy of the desingularized boundary integral method in free surface flow problems. In: *International Journal for Numerical Methods in Fluids* 25 (1997), Nr. 10, S. 1163–1184

[Lupieri und Contento 2015] LUPIERI, Guido ; CONTENTO, Giorgio: Numerical simulations of 2-D steady and unsteady breaking waves. In: *Ocean Engineering* 106 (2015), S. 298–316

[Mahboubidoust u. a. 2015] MAHBOUBIDOUST, Arash ; RAMIAR, Abas ; DARDEL, Morteza: Simultaneous Investigation of Flexibility and Plasma Actuation Effects on the Aerodynamic Characteristics of an Oscillating Airfoil. In: *Journal of Applied Fluid Mechanics* 9 (2015), 11

[Md Aktharuzzaman 2012] MD AKTHARUZZAMAN, MdShafiul Islam B.: Comparative Study of Flow Analysis over a National Advisory Committee for Aeronautics (NACA) 0012 Airfoil among Different Computational Methods with Experimental validation from Low Speed Subsonic Wind tunnel. In: *Military Institute of Science and Technology* 1 (2012), Nr. 1, S. 1

[Menter 1992] MENTER, Florian R.: Improved two-equation k-omega turbulence models for aerodynamic flows. (1992)

[Moser u. a. 1999] MOSER, Robert D. ; KIM, John ; MANSOUR, Nagi N.: Direct numerical simulation of turbulent channel flow up to Re τ= 590. In: *Physics of fluids* 11 (1999), Nr. 4, S. 943–945

[Prasad u. a. 2015] PRASAD, Bijoy ; HINO, Takanori ; SUZUKI, Kazuo: Numerical simulation of free surface flows around shallowly submerged hydrofoil by OpenFOAM. In: *Ocean Engineering* 102 (2015), S. 87–94

[Ridley 2014] RIDLEY, Chris J. Patterson Jonathan D.: *reeds Marine Engineering and Technology - Ship Stability Powering and Resistance Volume 13*. Bloomsbury Publishing, 2014. – URL `https://app.knovel.com/hotlink/toc/id:kpRMETSSP2/reeds-marine-engineering/reeds-marine-engineering`. – ISBN 9781408176122

[Te Chow 2013] TE CHOW, Ven: *Advances in hydroscience*. Bd. 1. Elsevier, 2013

[The OpenFOAM Foundation 2019] THE OPENFOAM FOUNDATION, OpenFoam: *vartical damping*. 2019. – URL `https://cpp.openfoam.org/dev/verticalDamping_8H_source.html`

[Tsai und Yue 1996] TSAI, Wu-Ting ; YUE, Dick K.: Computation of nonlinear free-surface flows. In: *Annual review of fluid mechanics* 28 (1996), Nr. 1, S. 249–278

[Walker u. a. 2004] WALKER, David T. ; ALAJBEGOVIC, Ales ; HUNT, Jason D.: Hydrodynamic Modeling for Stationary Breaking Waves / GENERAL DYNAMICS ADVANCED INFORMATION SYSTEMS DIV ANN ARBOR MI. 2004. – Forschungsbericht

[Wardle und Weller 2013] WARDLE, Kent E. ; WELLER, Henry G.: Hybrid multiphase CFD solver for coupled dispersed/segregated flows in liquid-liquid extraction. In: *International Journal of Chemical Engineering* 2013 (2013)

[Weller 2008] WELLER, Henry G.: A new approach to VOF-based interface capturing methods for incompressible and compressible flow. In: *OpenCFD Ltd., Report TR/HGW* 4 (2008)

[White u. a. 2011] WHITE, Frank M. u. a.: *Fluid mechanics*. Bd. 7. Mcgraw-Hill Education - Europe, 2011

[Wilcox 1988] WILCOX, David C.: Reassessment of the scale-determining equation for advanced turbulence models. In: *AIAA journal* 26 (1988), Nr. 11, S. 1299–1310

[Wilcox u. a. 1998] WILCOX, David C. u. a.: *Turbulence modeling for CFD*. Bd. 2. DCW industries La Canada, CA, 1998

[Yousefi und Razeghi 2018] YOUSEFI, Kianoosh ; RAZEGHI, Alireza: Determination of the critical Reynolds number for flow over symmetric NACA airfoils. In: *2018 AIAA Aerospace Sciences Meeting*, 2018, S. 0818